Faculty of Physics and Astronomy

University of Heidelberg

Diploma thesis

in Physics

submitted by

Thomas Pflüger

born in Landau in der Pfalz

August 2008

Electron Impact Single Ionization of Small Argon Clusters

This diploma thesis has been carried out by Thomas Pflüger at the

Max-Planck-Institute for Nuclear Physics

under the supervision of

Priv.-Doz. Dr. Alexander Dorn

Das Unendliche ist dort, wo der Unsinn vernünftig wird.[1]

Carl Friedrich v. Weizsäcker

[1]Infinity is, where nonsense becomes reasonable.

Zusammenfassung

Mit Hilfe eines Reaktionsmikroskops (RM) wurde die Ionisation durch Elektronenstoß von Argon Atomen und kleinen Argon Clustern, bei einer Projektilenergie von 100 eV untersucht. Es handelt sich hierbei um das erste (e, 2e) Experiment an Clustern und somit konnten zum ersten mal differenzielle Wirkungsquerschnitte gemessen und verglichen werden. Im Fall von atomarem Argon und Dimeren wurden vollständig differentielle Wirkungsquerschnitte (FDCS) bestimmt werden, für größere Cluster, einfach differentielle. Durch die Verwendung eines RM war es möglich, alle geladenen Fragmente in koinzidenz zu detektieren und somit ein kinematisch vollständiges Bild des Ionisationsprozesses zu erhalten. Der Vergleich der FDCS zeigte besonder in der zur Streuebene senkrechten Ebene signifikante unterschiede. Ar_2 wurde weiterhin auf mögliche Interferenzeffekte untersucht, die für Streuprozesse an diatomaren homonuklearen Molekülen vorrausgesagt werden. Es war möglich, Hinweise auf eine solche Interferenz zu finden, und diese mit einem einfachen Modell zu vergleichen. Hierdurch konnten weitere Einsichten in die unterschiedlichen Ionisationsprozesse zwischen Ar und Ar_2 gewonnen werden.

Abstract

Electron impact ionization of argon atoms and small argon clusters has been investigated at a projectile energy of 100 eV, using a so-called reaction microscope (RM). It is the first (e, 2e) experiment on clusters and therefore the first time differential cross-sections could be obtained and compared. For atomic argon and dimers fully differential cross-sections (FDCS) have been measured, for larger clusters, signly differential. With the use of a RM, it was possible to measure all charged fragments in coincidence and acquire a kinematically complete picture of the ionization process. The comparison of the FDCS showed the largest differences in the plane, perpendicular to the scattering plane. Furthermore, the ionization of Ar_2 has been studied for possible interference effects, which have been predicted for scattering processes on diatomic homonuclear molecules. It was possible to obtain first hints on such an interference structure and to compare it to a simple theoretical model. This also led to further insight on the different ionization processes for Ar and Ar_2.

Contents

1. Introduction

The interest in atomic and molecular collision experiments involving charged particles is on one hand deeply founded in the fundamental comprehension of modern physics. At the same time it is founded in the understanding of processes observable in nature like cosmic rays impinging on the atmosphere, but also in the interaction of biological organisms with radiation. A wide field of applications in medical science was created by the possibility of radiative treatment – both diagnostic and therapeutic – such as cancer therapy or X-ray examination. Even more interesting is the interaction of slow electrons with molecules since they are believed to play an important role for double string breaks of DNA in heavy ion therapy.
In recent years the interest in the properties of clusters increased rapidly. Since their bond is of the weak van-der-Waals type, they form an intermediate stage between isolated molecules and macroscopic systems. Therefore one is able to investigate the transition between the physical properties of free the participants up to condensed matter. In ordinary cluster experiments sizes of up to and above $40,000$ atoms or molecules are regarded. For $(e, 2e)$ experiments, however, clusters that large are far to complex and have too many reaction channels in order to derive quantitative results. Noble gas molecules – or van-der-Waals molecules – seem to be an obvious choice since they are comparably small with a manageable number of reaction channels, but at the same time show general properties of clusters.
Despite the deep knowledge about the structure of atoms and molecules – time independent atomic physics that is – many problems of dynamic processes remain unsolved. Problems of a static kind have been treated since the early beginnings of what we call modern physics, whereas time dependent problems are quite different. The fact that even a system of three particles cannot be solved analytically gives rise to theoretical methods which either rely heavily on assumptions about the described process or produce enormous computational efforts.
Collision experiments involving atoms or molecules are carried out since the early 1910s. When Rutherford, Geiger and Marsden performed the famous experiment emitting collimated particles from radioactive decay onto a thin layer of a solid (gold in this case). The detection of the scattered particles was done by a photoactive strip, bent circular with the foil in the center. The whole experiment was carried out in a coplanar geometry, where particles were detected only within a certain plane formed by the projectile beam and the circular strip. Since the strip had a certain width it defined the acceptance of the scattering geometry for particles being scattered to this plane. At the time, the intensity as a function of the scattering angle

was measured. The well-known outcome of the experiment was that the mass of an atom corresponded to its positive charge which was located in the center surrounded by a hollow shell of negative charges.
Since then there have been numerous collision experiments for all imaginable combinations of projectiles and targets such as electron-atom, ion-atom, photon-atom etc. With improved technology for detection devices, experimental setups grew more sophisticated. The development of quantum mechanics and the resulting knowledge about the structure of atoms and molecules lead to a broadened horizon for collision experiments. While in the original experiment of Geiger, Marsden and Rutherford the scattering was elastic, experimentalist where concerned with all kinds of inelastic scattering processes from excitation, multiple ionization to capture processes. Of course, in this scope the experimental techniques had to be improved to be capable of delivering detailed information. With the success of solid state physics in the field of semiconductors it was possible to create detectors capable of high resolution and high efficiency leading the way to the traditional $(e, 2e)$ apparatus where two energy sensitive detectors are used to detect the scattered particle and the ejected electron. This evolution, however, was still restricted to a certain plane where particles could be detected and – because of the spacial extension of the detectors – to certain *dead* regions, where the two detectors would overlap or one detector would block the incident beam. An important experiment for the evolution of the field of $(e, 2e)$ experiments was carried out by Ehrhardt in 1969, where an apparatus of the described type was used to measure single ionization of helium [17].
Spectrometers of this type are still being used with additional improvements to be able to detect so-called *out-of-plane* electrons, at least for certain solid angles. To cover larger out-of-plane parts, however, proves to be extremely difficult while an acceptance of 4π is almost impossible. It is not surprising that the experimentalists as well as theoreticians were focused on this coplanar geometry for decades. When the first experiments came to be where other planes were studied, the theoretical models which fitted well coplanar, suddenly completely failed in the description [34]. Therefore the invention of the reaction microscope was another milestone for atomic and molecular collision experiments [31]. Originating in recoil ion momentum spectroscopy the applied techniques have been developed to detect all charged particles created in a collision and gain full information about the process. Its advantage is the coverage of the whole solid angle which, at the same time, is accessible within one runtime of the experiment without adjusting detectors. For the first time three-dimensional fully differential data were available to compare to state-of-the-art theory. The impact of charged particles therefore provides a wide field of investigation. The possibility of obtaining the complete information of a particular process, such as all momenta, presents an additional possibility not only for better understanding but also as a test for contemporary theory.
In the present experiment the motivation of studying argon dimers was to investigate possible differences in the ionization process compared to atomic argon. Due to

the weak intermolecular bond strength ($\sim 15\,\mathrm{meV}$) the first approximation in order to describe an $(e, 2e)$ process would be to take Ar_2 as two independent atoms. The measurement of triply differential data on both Ar and Ar_2 provided information that indeed the dimer has to be looked at as a molecule.
The organization of the present work is as follows: an introduction into the field of $(e, 2e)$ experiments as well as a description of the properties of the studied targets will be given. Furthermore, a discussion of the most important theoretical models follows. The experimental setup will be presented in chapter 3, including a discussion of the acceptance and the resolution of the apparatus. Finally the outcome of the experiment will be presented. The separate analysis of the fully cross-sections at $E_0 = 100\,\mathrm{eV}$ impact energy for atomic argon as well as comparative discussion with triply differential cross-sections of Ar_2 of the obtained results are included. In the case of atomic argon a further comparison to contemporary theory will be shown. Lastly a summary of the results and an outlook for future experiments as well as improvements of the present will be given in in chapter 5.

2. Electron Impact on Atoms and Molecules

Processes which can occur when charged particles such as electrons scatter on atoms or molecules are quite numerous. This rich variety is usually divided into different classes depending on the final state particles. First of all one can decide whether or not the number of continuum particles changes. If the number of free particles remains constant and the energy is conserved, the scattering has been *elastic*. If the energy of the scattered projectile is not equal to its incident energy, the target could become excited which makes the process *inelastic*. Inelastic processes are then divided into pure excitation, pure ionization and a combination of both. For ionization and ionization-excitation the number of particles changes. Additionally, in the case of molecules, excitation of vibrational and rotational states, and dissociation is possible. Furthermore attachment processes – the capture of a free electron – can occur, which in the case of molecules, can also be dissociative (i.e. dissociative electron attachment or DA).
Electron impact ionization processes are usually denoted by the number of final state electron. For single ionization this would be $(e, 2e)$, for double ionization $(e, 3e)$ and so forth.

2.1. Electron Impact on Atoms

If electrons scatter on atoms, excitation to different energy levels is possible. Besides that, exchange effects can occur by which for instance ground state parahelium could be excited to orthohelium, while ionization to positive ions in different charge states (e.g. *singly*, *doubly* etc.) is also possible. Of course, electron capture is another possibility, thus forming a negative ion.
A characteristic property of such processes is the total *cross-section*, being the probability for a reaction to occur, usually plotted as a function of the projectile energy. For the above mentioned processes, the order of magnitude of the cross-section can be quite different even for the same reaction in different atoms. To get a deeper knowledge about the kinematics in a given reaction it is often not useful to look just at the total probability, but at the probability dependence as a function of different kinematic variables, such as energy and scattering angle. In that sense the *total*

cross-section (TCS) contains the least information.[1] This is due to the fact that the TCS is the integral of a differential cross-section over all kinematic dependencies. The order of the differential is dependent on the specific process, meaning, how many variables are needed to determine the reaction completely. For instance the pure single ionization of an atom has a three-fold differential cross-section often referred to as the *triply differential* - (TDCS), whereas double ionization has a five fold differential cross-section. More generally one can simply speak of the fully differential cross-section (FDCS). The TDCS for single ionization is defined by the solid angles of the two outgoing electrons and the energy of one electron). For an experimentalist the FDCS is the fundamental variable since there would be no possibility to acquire differential data when only the TCS was measured.
Usually in an $(e, 2e)$ experiment, the determination of the FDCS is achieved by fixing the scattering angle of the projectile with one spectrometer. This characterizes the scattering plane: A plane which is spanned by the momentum vectors of the projectile before and after the scattering. Secondly, the energy of the ejected electron has to be fixed with a second spectrometer. In conventional experiments, obtaining the number of counts as a function of the ejection angle of the second electron in coincidence with the scattered projectile within this plane gives the FDCS.[2] Since the ejection of an electron is not only limited to this plane, one could think of complementary planes, such as the *perpendicular plane*. It is defined as a plane, orthogonal to the scattering plane, containing the projectiles momentum vector. Of course, every other plane between those two is imaginable, but with traditional setups, hardly obtainable.
Nevertheless, it's worthwhile to gain as much information as possible about a spe-

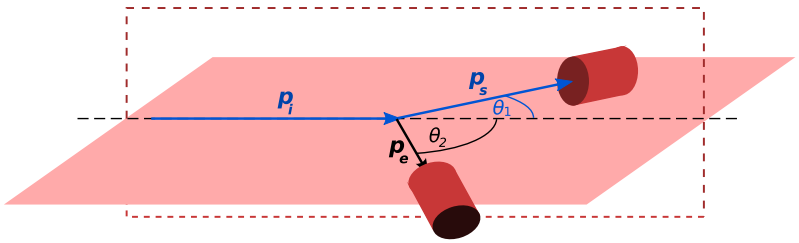

Figure 2.1.: Conventional $(e, 2e)$ experiment. Shown in red (solid) is the scattering plane, with the momenta for the projectile (p_i), the scattered projectile (p_s), the ejected electron (p_e) and their respective scattering angles. Indicated in dashed red is the perpendicular plane.

[1] i.e.: *For which incident energy the reaction is most probable.*
[2] Detecting ejected electrons in the scattering plane defines the *coplanar geometry.*

cific process and particularly the RM offers the possibilities to obtain a complete picture, which is not restricted to a certain plane, but covers the whole solid angle (see section 3.1).
Generally speaking, the characteristic features of a FDCS in an $(e, 2e)$ experiment can be separated into two aspects. The projectile can scatter with small impact parameter and mainly interact with a bound electron where the remaining ion is merely a spectator. This kind of collision is called *binary* and the respective peak in the FDCS is therefore called binary peak. Most likely the electron will then be ejected in the direction of the momentum transfer ($\vec{q}$). On the other hand – if the projectile has large impact parameter and the energy and momentum transfer is small – there is a probability that the emitted electron interacts with the remaining ion, causing it to scatter in the opposite direction. This peak in the FDCS is called *recoil peak*. In figure 2.2(b) a FDCS for helium is shown and one can see the charac-

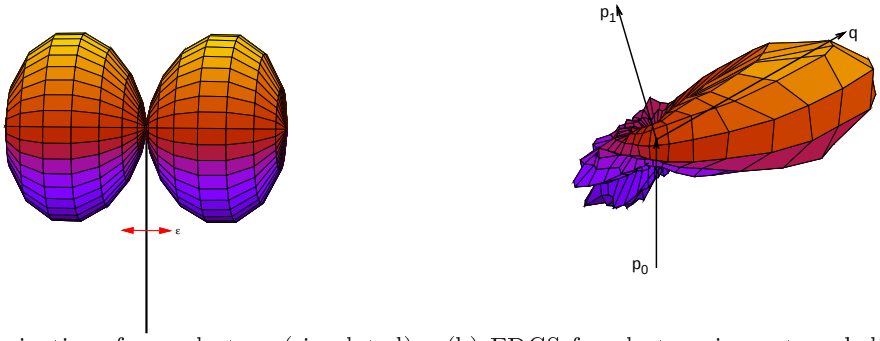

(a) Photoionization of an s-electron (simulated).

(b) FDCS for electron impact on helium at eV incident energy.

Figure 2.2.: Difference between electron impact ionization and photoionization processes.

teristic *double lobe* structure, where the large lobe in the direction of $\vec{q}$ corresponds to the binary peak and the smaller one in the opposite direction to the recoil peak. In the limit of an infinitesimal momentum transfer one would expect the lobes to be symmetric around the direction of the projectile. This would then correspond to photoionization where the momentum transfer is negligibly small (2.2(a)).

2.1.1. Atomic Argon

For this work, atomic argon has been chosen as an additional target. Compared to dimers where molecular binding energies are weak, it was one aim of this work to see whether or not the presences of a second bound atom would play a significant

role in the ionization process.
The valence electrons in argon are p - electrons with an ionization potential (IP) of 15.94 eV for a remaining $^2P_{1/2}$ ion and 15.76 eV for a $^2P_{3/2}$ ion.[3] Due to the energy resolution of the setup, the different P states cannot be resolved. For the ionization of a s - electron - leading to $^2S_{1/2}$ - the IP is 29.35 eV (all [33]). The overall contribution of the $3s$ shell can be considered small compared to the $3p$ shell. In the energy range of around 100 eV for the projectiles, their contribution is in the order of 6% [22].
For the excitation of argon by electron impact, there exists an considerable amount of possible states. Due to the magnitude of the cross-section at this projectile energy, only the excitation of a $3p$ - electron will be taken into account. Since the cross-sections of excitation into s - states are small, the first set of states are ten $3p^5 4p$ - states [24]. In the Paschen notation they are usually denoted by $3p^5(n+2)p$ with the addition of the total angular momentum $J = 0, 1, 2$, making the individual states $2p_i$ ($i = 1...10$). They are spread between the lowest, $3p^5(^2P_{3/2})4p$ (or $2p_{10}$), at 13.01 eV and the highest, $3p^5(^2P_{1/2})4p$ (or $2p_1$), at 13.59 eV above the ground state. The next set of states, $3d$, start at 13.96 eV (see section A.2). Excitation by electron impact of argon has been studied intensively and measured cross-sections can be found e.g. [9], [10]. Is has been shown that by an incident energy of 100 eV, $2p_1$ has the highest partial cross-section of $(25 \pm 5) \cdot 10^{-19}\,\mathrm{cm}^{-1}$, while the total excitation cross-setion into $2p_i$ is $(107.2 \pm 12.1) \cdot 10^{-19}\,\mathrm{cm}^{-1}$ [9]. For comparison, the combined cross-section for excitation into $3d_i$ and $2s_i$ is $(9.68 \pm 2.37) \cdot 10^{-19}\,\mathrm{cm}^{-1}$ [10].
The total cross-section for electron impact ionization has been measured to be in the order of $2.5 \cdot 10^{-16}\,\mathrm{cm}^2$ for 100 eV incident electron energy [28]. Singly charged Ar, with an IP of 27.63 eV, for the configuration $3s^2 3p^5\ ^2P_{1/2,\,3/2}$, has a significant set of $4p$ - states, starting 19.38 eV above the ground state, for the term $^4P_{5/2}$. Another set would be the $3d'$ - states at ~ 21.7 eV and the $4d$ - states, starting at ~ 22.8 eV. One should note that all excitation cross-section for those states, peak a 100 eV, with magnitudes in the order of $\sim 10^{-19}\,\mathrm{cm}^2$ [38]. Compared to helium, for atomic argon one should be able to see distinct differences in the fully differential data. Since the valence electrons in Ar have an initial momentum, there should be a suppression of ejected electrons with a momentum $\vec{q}$, in contrast to He, where the s - electrons have no initial momentum. Since this initial momentum adds to the transferred momentum gained in the collision, one should see a minimum for Ar in the direction of the momentum transfer. Also, because of the higher core charge, second order effects can occur, where the projectile before or after interaction with a bound electron, gets elastically scattered on the core. This would then move ejected electrons slightly out of the scattering plane or to different scattering angles within, leading to a more blurred distribution. This is a reason, why the perpendicular plane is of particular

[3] The configuration is $(1s)^2(2s)^2(2p)^6(3s)^2(3p)^6$

interest, comparing experimental results with theory. Since the probability for an electron to be ejected to the perpendicular plane is much smaller compared to the ejection to the scattering plane. With this difference in magnitude, the perpendicular plane is much more sensitive to small, second (or higher) order effects. Hence, there can be some discrepancy between theory and experiment in the perpendicular plane, even when they match well in the coplanar plane. This effect has been observed before in electron and ion impact experiments [34], [16].

2.2. Electron Impact on Molecules

Since molecules have more internal degrees of freedom, not only can they be excited to different electronic states, but also to a rich variety of vibrational and rotational states. It is now possible to excite to different vibrational states within the same electronical state, excitation to the same vibrational state in different electronic states and of course excitations between different vibrational states in different electronical states. The overall probability of an excitation to a different state is described by the Franck-Condon principle. It says that the excitation process takes place so fast that the internuclear distance doesn't change (e.g. [13]). Therefore, the most probable transition is to a vibrational state for which the probability distribution for the intermolecular distance is large. For the lowest vibrational state this is usually the center of the potential curve whereas for excited vibrational states it is at the turning points of the vibration. Another distinctive difference between atoms and molecules are dissociative processes. They occur, when the molecule is excited a anti-bound state or to a vibrational continuum state, where the internuclear distance gets so large that the participants finally part. Another possibility for dissociates via the coupling between electronic states. If the potential surfaces of electronic states intersect it is possible that the molecule which has been excited to a bound state, dissociates via coupling with another electronic state, for which the energy is already in the vibrational continuum. This is usually called predissociation. In order to ionize a molecule, the energy has to be sufficient not only to overcome the dissociation limit but to reach the desired electronic state. Also, due of the Franck-Condon principle, it is not likely for a molecule, to be ionized to a vibrational ground state. Since the internuclear equilibrium distances can be quite different for the neutral and ionized molecule, due to the different charge, the largest Franck-Condon factors are obtained for higher vibrational states of the ion.

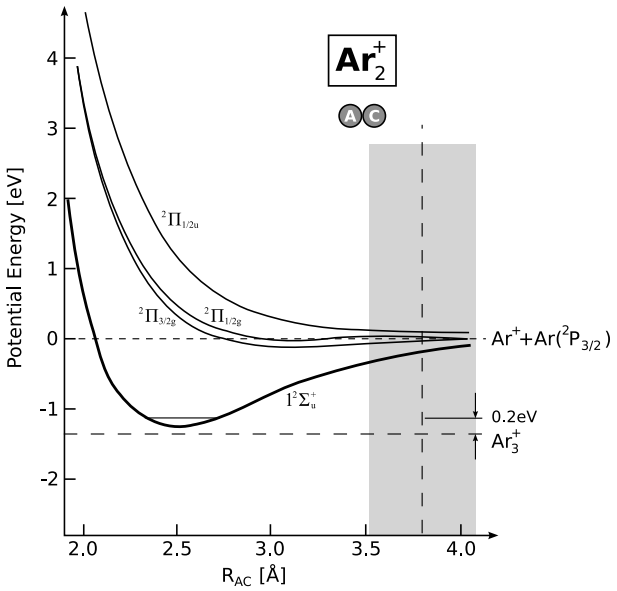

Figure 2.3.: Potential curves for different states of Ar_2^+ with Franck-Condon (grey shaded) region for ground state ionization [26]. The dashed horizontal line indicates the Ar_3^+ ground state.

2.2.1. Argon Clusters

The primary target in this work was Ar_2, which is a noble gas dimer. Generally speaking, this type of *clusters* are molecules which are bonded through the long range van-der-Waals force. The overlap of the electronic orbitals gives rise to a repulsive exchange interaction, leading to a relatively low bond strength. The bond itself is created by induced dipole interaction between neutral participants. Due to the small binding energy, the potential surfaces of van-der-Waals clusters are very shallow, containing only a limited number of vibrational states. Dissociation of such a cluster requires only a small amount of energy, exciting it to a vibrational continuum. For argon dimers, the dissociation energy is only $\sim 13\,\mathrm{meV}$, where the intermolecular distance is $\sim 3.8\,\text{Å}$.
Figure 2.3 shows particular electronic states of the argon dimer ion, with the Franck-Condon region for ionization from the neutral ground state. Since the gas jet has a low temperature we can assume that Ar_2, Ar_3 and larger cluster are initially not vibrationally excited. This is of particular importance since it ensures a well prepared target and an enhanced momentum resolution.
Experimentally the observation was focused on the detection of Ar_2^+ ions. The reason for this was besides studying argon dimers that among the atomic targets, the number of dimers was already low resulting in a low count rate and thus the

percentage of larger clusters ($Ar_n,\ n > 4$) was assumed to be negligibly small. Secondly, it has been shown that by electron impact ionization of size selected Ar_3 and Ar_4, there is no significant production of the respective ions and furthermore that there is even no significant creation of Ar_3^+ ions by electron impact ionization of Ar_4 [4]. Following ionization, all of those species dissociate into dimer ions plus neutrals, since these products are energetically favored compared to the trimer ion states.[4] Therefore, focusing on dimer ions makes it possible to obtain information about the ionization of larger argon clusters. Figure 2.4 shows calculated potential energy curves of the trimer ion in different geometries. The zero point has been chosen to be the dissociation into $Ar^+ + 2Ar$. The geometrical structures of neutral

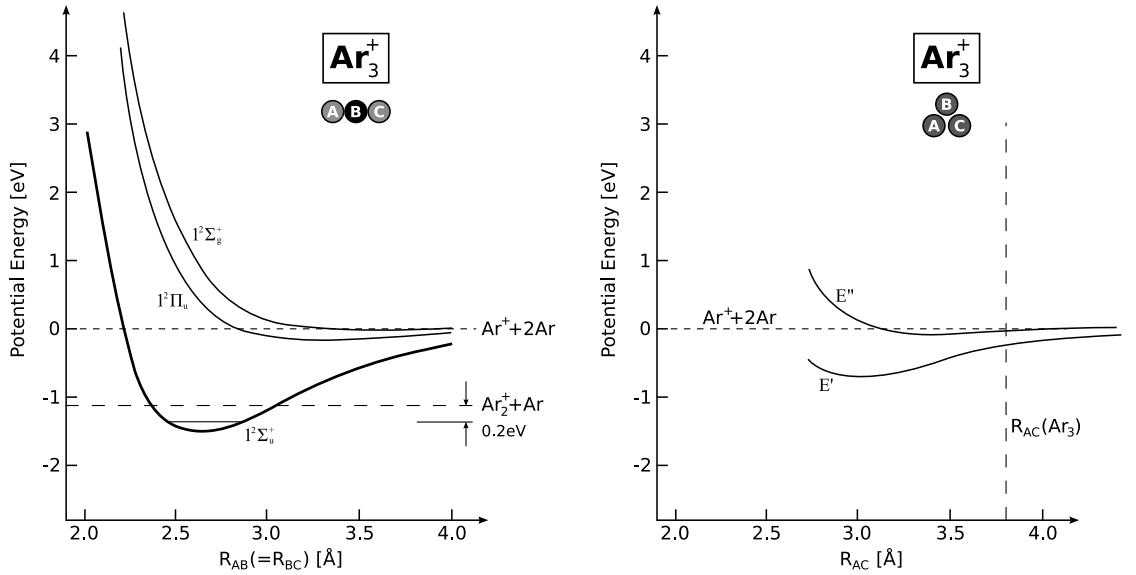

(a) Potential curves for different states of Ar_3^+ with linear geometry and equal bond lengths ($D_{\infty v}$).

(b) Potential curves for different states of Ar_3^+ with equilateral triangle configuration (D_{3h}). The vertical line indicates the Ar_3 equilibrium distance.

Figure 2.4.: Calculated potential energy curves for Ar_3^+ in different geometry [27]

trimer and ionic trimer are quite different. For Ar_3 it has been shown that the configuration with the lowest energy is an equilateral triangle with an internuclear distance of 3.8 Å (e.g. [18]), whereas for Ar_3^+ the most stable configuration is linear, with the center carrying 50% of the charge, and for larger clusters Diatomics in molecules (DIM) calculations have shown that the ions are formed by a trimer ion core surrounded by neutral atoms [21]. The predicted configuration for the trimer ion is therefore linear with an internuclear distance of 2.6 Å as shown in figure 2.4(a). As a result, the ionization of a neutral trimer leads to ions in a non-

[4]It has been stated that stable Ar_3^+ is only produced by Ar_5 and larger clusters [4].

equilibrium configuration, which are therefore rather *hot* (see figure 2.4(b)). The energy difference of the linear trimer ion compared to the triangular configuration is in the order of 1.0 eV. Since the dissociation limit into Ar_2^++Ar is only 0.2 eV above the ground state in the $D_{\infty v}$ configuration, it can already dissociate.

Compared to the direct ionization of Ar_2, the momentum balance is now different

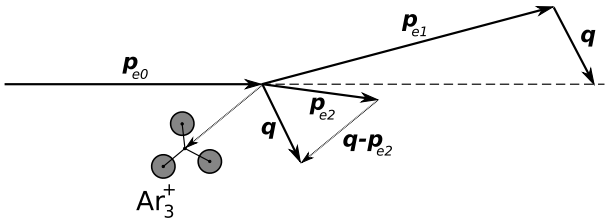

Figure 2.5.: Ionization scheme for Ar_3 prior to dissociation. The momentum transferred to the trimer ion has been denoted as $\boldsymbol{q}$ - $\boldsymbol{p}_{e2}$.

for Ar_3. Shown in figure 2.5 is a scheme of the initial ionization process. In a first step, the trimer is ionized, and the momentum transferred to the trimer ion and the ejected electron is $\vec{q}$. Finally, the trimer ion dissociates into a dimer ion and a neutral. The momentum transferred to Ar_3^+ is not the measured $\vec{p}_r$, but the momentum transfer $\vec{q}$ minus the momentum of the second, ejected electron $\vec{p}_{e2}$. In the rest frame of the initial ion (i.e. Ar_3^+), the momentum of the dimer ion is now given as

$$\vec{p}_r\,' = \vec{p}_r - \frac{2}{3} \cdot (\vec{q} - \vec{p}_{e2})\,, \tag{2.1}$$

while the neutral fragments momentum is

$$\vec{p}_n\,' = \vec{p}_n - \frac{1}{3} \cdot (\vec{q} - \vec{p}_{e2})\,. \tag{2.2}$$

The fraction of the transferred momentum is due to the asymmetric mass separation in the dissociation process. Of course, since the neutral fragment hasn't been measured, its calculation wont provide any information which isn't contained in the other charged fragments kinematic variables. However, due to the dissociation process and hence the additionally gained momentum, one should be able to observe a broad structure in the time-of-flight spectrum for the ions.

		R_{B-AC}[Å]	R_{AC}[Å]	E_{diss} [eV]	E_{IP} [eV]	diss. channel
Ar_3^+	1	0.000	5.229	-1.3762	-	$Ar^+ + 2Ar$
	2	2.237	3.317	-0.7010	-	
Ar_3	-	2.171	3.760	-0.0373	14.370	
Ar_2^+	-	-	2.450	-1.1790	-	Ar^++Ar
Ar_2	-	-	3.762	-0.0122	14.500	

Table 2.1.: Summarized data of small argon cluster [6],[27],[39]

2.2.2. Interference Effects on Diatomic Molecules[5]

The wave nature of particles is one of the most prominent derivations in quantum mechanics, leading to a number of results, unimaginable in classical physics. Interference pattern are always expected, when particles behave like waves. This means, whenever - for the same result - different paths are available and on principle one cannot determine which path a particle had been taken, the wave-nature of particles shows up and interferences is possible. For photons, this effect has been known since Young's double-slit experiment in 1802.[6] However, to create the same experiment for electrons took some 160 years and was performed by Claus Jönsson in 1961 [23]. For the underlying principle it doesn't matter, whether the physical process is diffraction on a double-slit or scattering, if one cannot know which path of the particles, interference pattern are observed. In particular if one thinks of scattering processes, a homonuclear diatomic molecule would be ideal since the projectile can scatter at any of the two participants. This has been a long standing prediction for photoionization by Cohen and Fano, done in the late sixtes [11]. More recently, theoretical predictions have been made, concerning the single ionization of molecular hydrogen by electron impact [36].

Figure 2.6 shows a schematic view of such a scattering process. For a given orientation of the molecular axis one cannot distinguish which path the projectile took. If the distance between the two scattering centers is large, the Hamiltonian can be expressed as the sum of the two atomic Hamiltonians plus the interaction potentials between an atom and the incoming particle. The transition amplitude can than be expressed as

$$\hat{T} = V + V\hat{G}_0 V + \dots \ , \tag{2.3}$$

[5]The equations of this section are in atomic units.

[6]Originally, the purpose of this experiment was to prove the wave nature of light.

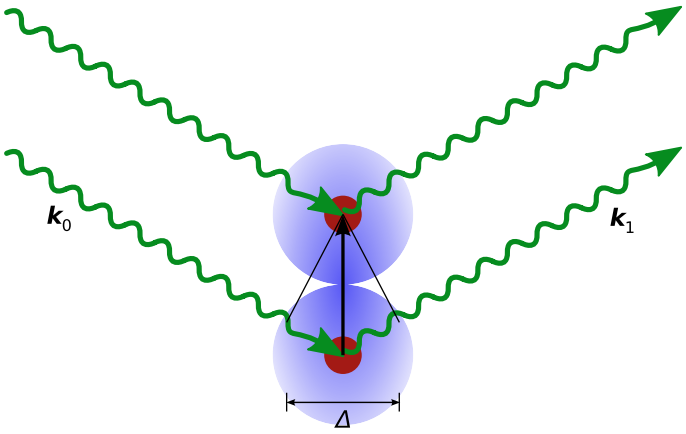

Figure 2.6.: Interference on a homonuclear diatomic molecule.

where $\hat{G}_0$ is Greens operator and $V = V_1 + V_2$ is the sum interaction potentials between the particle and the respective atom (see section 2.3.1). The phase difference between the incoming and the scattered wave can be expressed as

$$\Delta = (\vec{p}_0 - \vec{p}_1) \cdot \vec{R} \,, \tag{2.4}$$

where $\vec{R}$ is the intermolecular distance vector and $\vec{p}_i$ are the respective electron momenta, prior to and after the scattering. If the scattering process is elastic, the differential cross-section is

$$\frac{\mathrm{d}\sigma_{A_2}}{\mathrm{d}\Omega} = \frac{\mathrm{d}\sigma_{2A}}{\mathrm{d}\Omega} \left[1 + \cos(\vec{q} \cdot \vec{R})\right] . \tag{2.5}$$

The term in brackets is called, as an interference term. If there would be no interference, the differential cross-section for the two targets would just be the sum of the individual differential cross-sections.
For inelastic scattering on a molecule, the relation follows equation 2.5 [37]:

$$\mathrm{d}\sigma_{A_2} = \mathrm{d}\sigma_{2A} \left[1 + \cos(\,(\vec{p}_{e2} - \vec{q}) \cdot \vec{R})\right] , \tag{2.6}$$

and if the molecular axis is not oriented, additionally, one has to average over all possible orientations, leading to

$$\mathrm{d}\sigma_{A_2} = \mathrm{d}\sigma_{2A} \left(1 + \frac{\sin(|\vec{p}_{e2} - \vec{q}\,|R)}{|\vec{p}_{e2} - \vec{q}\,|R}\right) , \tag{2.7}$$

where $R = |\vec{R}|$ is the absolute distance between the two nuclei. However, one should note that in contrast to the derived result for elastic scattering, two independent atoms are not sufficient to observe interference. For a given molecular axis one would then be able to have *which way* information, since the inelastic scattering process on one atom or the other can be seen as flagging the particular target, hence destroying the interference pattern. The target electron must not be assigned to one of the target nuclei.

2.3. Theoretical Background

The problem of the theoretical description of an $(e, 2e)$ process is that even the simplest single ionization by electron impact - the ionization of hydrogen - is a three-body process and therefore not analytically solvable. Theoreticians have developed a number of different methods to get a hold to this problem. Dating back to the early 30's, Bethe and Born developed the first quantum mechanical approach for inelastic atomic scattering. In principle one could divide them into *perturbative* and *non-perturbative* approaches. For perturbative approaches (e.g. Born approximation), one must carefully decide whether or not the interaction of the projectile with the target system is small and whether or not higher order effects have to be taken into account. In those models, the scattering process is divided into an initial and final state, the interaction between projectile and target is treated separately. This applies only for *fast* projectiles, whereas slow collision can hardly be treated pertubatively. On the other hand, those methods work well also for heavy atoms.
Non-perturbative approaches, however, are based on a numerical solution of the Schrödinger equation (e.g. convergent close-coupling). They are best suited for low projectile energies, but, at the same time, are somewhat restricted to light targets. Nevertheless, in this scope, they have shown to deliver excellent results, justifying the enormous computational effort.
Among the large variety of different theoretical descriptions, only the most important ones will be taken into consideration.

2.3.1. Born Approximation

To solve a problem like electron impact ionization pertubatively, usually the system's Hamiltonian is divided in the projectile, the target and the interaction term (e.g. [32]). This means that projectile and target remain independent, prior and after the interaction. Since the Coulomb interaction has an infinite range this is already a strong approximation. The Hamiltonian can be expressed like

$$\hat{H} = \hat{H}_0 + \hat{W} \ , \tag{2.8}$$

with the unperturbed Hamiltonian $\hat{H}_0 = \hat{H}_{target} + \hat{H}_{projectile}$. The interaction between the target and the projectile is now only due to the interaction potential $\hat{W}$ which - if considered small - remains a perturbation to the otherwise free system. Therefore the initial state of the system is just the product of the free projectile, which can be written as a plane wave (e.g. $\langle \vec{x} \,|\phi_i\rangle = \exp[i\vec{k_i} \cdot \vec{x}/\hbar]/(2\pi\hbar)^{3/2}$) and the target system (e.g. $|\psi_i\rangle$). The initial and final states are expressed by $|i\rangle = |\phi_i\rangle \otimes |\psi_i\rangle \equiv |\Psi_i\rangle$ and $|f\rangle = |\phi_f\rangle \otimes |\psi_f\rangle \equiv |\Psi_f\rangle$ and they are eigenstates of $\hat{H}_0$:

$$(\hat{H}_0 - E)\,|\Psi_{if}\rangle = 0\ .^{7} \tag{2.9}$$

The eigenstates of $\hat{H}$ shall be given by

$$(\hat{H} - E)\,|\Phi_{if}\rangle = 0\ . \tag{2.10}$$

A possible, formal solution to equation 2.10 can be given by

$$|\Phi_{if}\rangle = |\Psi_{if}\rangle + \hat{G}_0\hat{W}\,|\Phi_{if}\rangle\ , \tag{2.11}$$

where $\hat{G}_0$ can be identified with the Green operator

$$\hat{G}_0 = \lim_{\epsilon\to 0} \frac{1}{E - \hat{H}_0 + i\epsilon}\ .^{8} \tag{2.12}$$

Still the function $|\Phi\rangle$ on the right hand side of equation 2.11 - which is known as the Lippman-Schwinger equation - remains unknown.
By iteratively inserting 2.11 into itself, one can push back this function to higher order elements. The probability for a transition is defined by means of the transition matrix ot t-matrix. One can derive the so called Born series, by inserting the Lippman-Schwinger equation into

$$T_{if} = \langle \Phi_f |\,\hat{W}\,|\Phi_i\rangle = \langle \Psi_f |\,\hat{W}\,|\Psi_i\rangle + \langle \Psi_f |\,\hat{G}_0\hat{W}\hat{G}_0\,|\Psi_i\rangle + \ldots\ . \tag{2.13}$$

The first order Born approximation or first Born transition amplitude is now given by

$$f_{if}^{(1)} = \langle f |\,\hat{W}\,|i\rangle \equiv \langle \Psi_f |\,\hat{W}\,|\Psi_i\rangle\ . \tag{2.14}$$

One can show that the cross-section can be acquired from the transition amplitude: $\sigma \propto |f_{if}^{(1)}|^2$. For electron impact the interaction can be expressed like

$$\hat{W} = -\frac{Z_{pr}Z_{ta}}{R} + \sum_{i=1}^{N} \frac{Z_{pr}}{|\vec{r}_i - \vec{R}|} \tag{2.15}$$

[7] The indexing is kept to a minimum, in order not to be cumbersome.
[8] Here, $\hat{G}_0$ is defined positive to ensure the scattered wave is outgoing.

with $\vec{R}$ the distance between projectile and target and $\vec{r_i}$ the distance between the nucleus and the target electrons. Combination of equations 2.14 and 2.15 leads to

$$f_{if}^{(1)} = \frac{Z_{pr}}{2\pi^2 q^2} \langle \phi_f | \sum_{j=1}^{N} \exp[\, i\vec{q} \cdot \vec{r}_j \,] \, | \phi_i \rangle \ , \tag{2.16}$$

where the momentum transfer $\vec{q} = \vec{k}_f - \vec{k}_i$ is introduced.
As for higher order Born approximation the complexity of solving increases rapidly, the second Born amplitude can be expressed as

$$f_{if}^{(2)} = \lim_{\epsilon \to 0} \langle \Psi_f | \, \hat{W} \frac{1}{E - \hat{H}_0 + i\epsilon} \hat{W} \, | \Psi_i \rangle \ , \tag{2.17}$$

which accounts for the fact that the system can undergo a second transition during the reaction. For the second Born approximation, the cross-section is obtained by

$$\sigma \propto |f_{if}^{(1)} + f_{if}^{(2)}|^2 \, . \tag{2.18}$$

As mentioned before, the computational difficulty increases rapidly with the order of approximation. Therefore, there are hardly any cases, where higher order Born approximations are reachable.

2.3.2. Distorted Wave Born Approximation (DWBA)

As an extension to the previously described Born approximation, the distorted waves method takes into account that often particularly the Coulomb interaction between the projectile and the target system, cannot be neglected due to its infinite range and therefore the projectile cannot be treated as a plane wave. To take this interaction into consideration, while still ensure the problem to be solvable, an additional operator is introduced. The complete interaction potential is therefore expressed as

$$\hat{W}_{if} = \hat{U}_{if} + \hat{V}_{if} \ , \tag{2.19}$$

where the subscript denotes whether the potential describes the initial or the final state (e.g. [2]). The first term in equation 2.19, $\hat{V}_{if}$ are (small) perturbations, describing the interaction, whereas $\hat{U}_{if}$ are the so-called *distortion* terms, describing the coulomb interaction. These potentials are to be understood in a way that

$$\hat{H} = \hat{H}_0 + \hat{U}_{if} \tag{2.20}$$

$$\hat{H}' = \hat{H} + \hat{V}_{if} \, . \tag{2.21}$$

A solution is now obtained by solving equation 2.11 for $\hat{U}_{if}$,

$$|\chi_{if}\rangle = |\phi_{if}\rangle + \hat{G}\hat{U}_{if}\,|\chi_{if}\rangle \ , \tag{2.22}$$

obtaining the eigenfunctions for the distortion interaction in the initial and final state. The transition amplitude can now be written as,

$$T_{if} = \langle\chi_f|\,\hat{U}_f\,|\Psi_i\rangle \tag{2.23}$$

$$= \langle\Psi_f|\,\hat{U}_i\,|\chi_i\rangle \ , \tag{2.24}$$

which is referred to as *post* and *prior* form.
If the perturbation $\hat{V}_{if}$ is small, one could argue, so is the difference between $\hat{H}'$ and $\hat{H}$, or their respective eigenstates. Up to now, no Born approximation has been applied. This is done - in first order - following the previous argument, by substituting

$$|\Psi_i\rangle \to |\chi_i\rangle \ . \tag{2.25}$$

The advantage of this method is that for a complex situation like ionization by charged particle impact, the problem with combined interaction of the coulomb field and the *direct* interaction between the projectile and the active electron, is hardly solvable. Unfortunately, especially for low energy scattering, neglecting the coulomb interaction is a poor choice.[9] Therefore, one can at least partly treat both problems, by shifting them to different potentials. Of course, how this is finally applicable has to be determined, in which way the problem is easier to solve (i.e. for $\hat{H}$ or for $\hat{H}'$).
In recent years, a number of improvements to the *DWBA* have been developed, such as *DWBA*-G, which is corrected by the Gamow factor for improved PCI ([25]) and hybrids like *DWBA*-RMPS, which is a combination of DWBA (first or second order), the R-matrix approach and a *pseudo-state* close-coupling-type expansion ([3]).

2.3.3. Convergent Close-Coupling

In the convergent close-coupling approach the time-independent Schrödinger equation is solved numerically in an non-perturbative way. Initially it was developed to describe the $2p$ excitation of atomic hydrogen but was later extended to describe also - among other - the ionization of hydrogen and helium by electron impact [7]. Solutions are found by diagonalizing the target Hamiltonian with a set of Laguerre polynomials, which results in a set of N target states. These are often referred to as *pseudo states*. Here N indicates the size of the basis set. With an increasing basis size the target states (e.g. $|\psi_i\rangle_N$) converge to the discrete eigenstates for negative energies whereas for positive energies they form a dense pseudo continuum.

[9] E.g. due to *post collision interaction* (PCI).

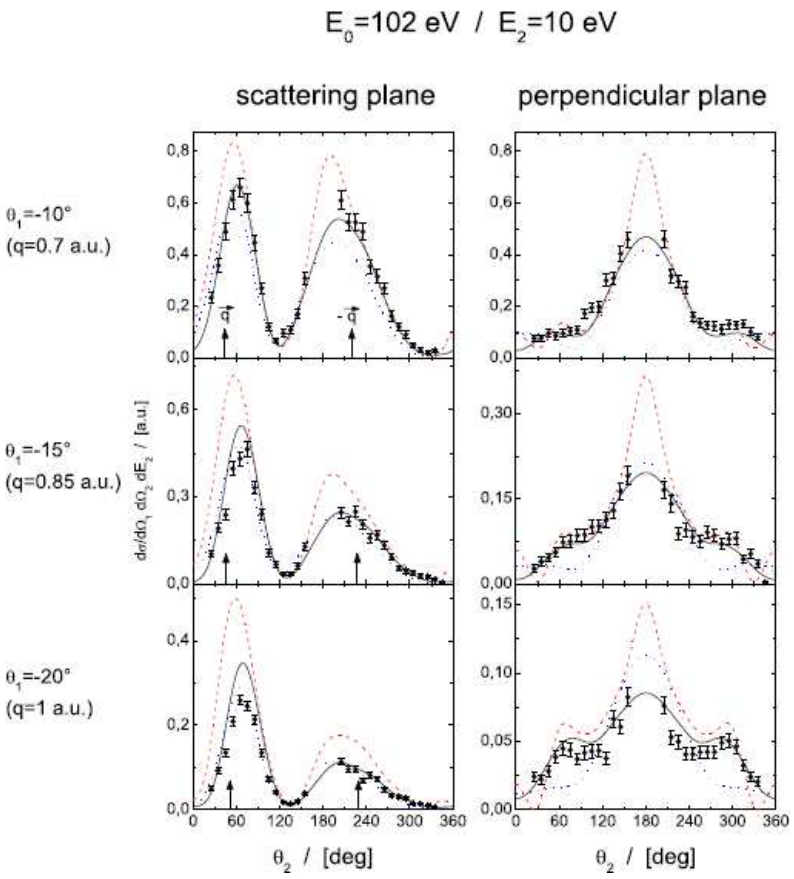

Figure 2.7.: FDCS for $(e, 2e)$ on helium at 102 eV projectile energy. Theoretical calculations shown are CCC (–), DWB2 (- -) and 3C (···) [15].

The fact that the bound electron is excited to a pseudo continuum state has caused some controversy since the two electrons should be indistinguishable, but it could be shown that even for the case that both electrons share the same energy agreement with experiments is very good ([5], [35]).
A major drawback of CCC is that it works well only for light atoms and even for helium the approximation of a *frozen core* – an assumption which *freezes* all electrons except the active one – has to be made.

2.3.4. *R*-Matrix Approach

In the R-matrix approach, the problem of indistinguishability between the projectile and the target electrons is overcome by separating the space into an area, where the projectile is far away from the target and an area where the indistinguishability can no longer be neglected. In a first step the problem of the approaching and scattered projectile can then be solved exactly, while only the interaction within an enclosed volume has to be treated with more sophistication. This makes perfect sense since the same problem can be solved much easier on small scales, than within a large scale frame.
The surface, separating the inner from the outer region is usually a sphere of radius a. The inner part of the problem is treated with as much as possible complexity in the interaction, describing the basis-state wavefunctions as an expansion of continuum orbitals and target wavefunctions. For molecular ionization processes at low to intermediate energies, the description is restricted to a *fixed nuclei* approximation, where the nuclear motion is neglected and the electronic states are obtained for the equilibrium distances. The target wavefunctions can be acquired by configuration interaction methods (e.g. CASS(D/T), CASCI) . The molecular orbitals, as well as the continuum orbitals, are expanded in Gaussian-type orbitals (GTO), whereas the basis sets are obtained by a finite-range fit of Bessel or Coulomb functions. It should also be mentioned that usually – in many-electron molecules – tightly bound electron pairs are fixed for the duration of the reaction, performing these types of calculations [19].
As for the RMPS, parts of the target wavefunctions are expressed as *pseudo states*, using a close-coupling expansion (see section 2.3.3). In order to ensure that the pseudo-continuum truly represents the post-ionization configuration, the ejected electron is described by a set of so-called *pseudo-continuum orbitals* which are introduced to the configuration-interaction.

3. Experimental Setup

This chapter describes the basic apparatus used and the experimental techniques applied to measure the fully differential cross-section (FDCS) for single ionization of Ar_2 by electron impact. The reaction microscope (RM) which was used in this experiment provides the opportunity of obtaining the kinematically complete information about the process [31]. It is hereby possible to cover almost the complete solid angle and a large range of energies during one measurement, whereas with conventional spectrometers it was only possible measure one angle and electron energy at a time. This technique is based on high resolution position sensitive detectors and the ability to detect all charged fragments produced.
In contrast to a conventional spectrometer for this kind of experiment where the FDCS is obtained directly by aligning two detectors and changing their angles respectively, a RM collects all the particles first and the reconstruction (or the 'imitation' of a conventional spectrometer) is done during the data analysis.

3.1. The Reaction Microscope

As mentioned before, a reaction microscope was used for the detection. A schematic view can be seen in figure 3.1. The gas jet and the incident electron beam are crossed under 90° in the center between the spectrometer plates. The direction of the magnetic field produced by the Helmholtz coils is parallel to the spectrometer axis.

The spectrometer plates produce a homogeneous electric field anti-parallel to the magnetic field. This field accelerates the charged fragments to opposite directions regarding their charge. The acceleration region – within the extent of the plates – is followed by a drift region without an electric field. The purpose of the electric field is simply to image the particles onto the detectors. The magnetic field confines the electron's radial movement and forces them on cyclotron trajectories. This is necessary for electrons with large transversal momentum to still hit the detector. Because the mass of the ions is four orders of magnitudes larger the influence of the B-field on their trajectories is negligible.
The principle of this apparatus is to reconstruct all charged particles' momenta by measuring the respective times of flight and positions on the detectors. Hereby the longitudinal momentum is connected to the time a particle needs to reach the detector, whereas for the transversal momentum the position on the detector is needed

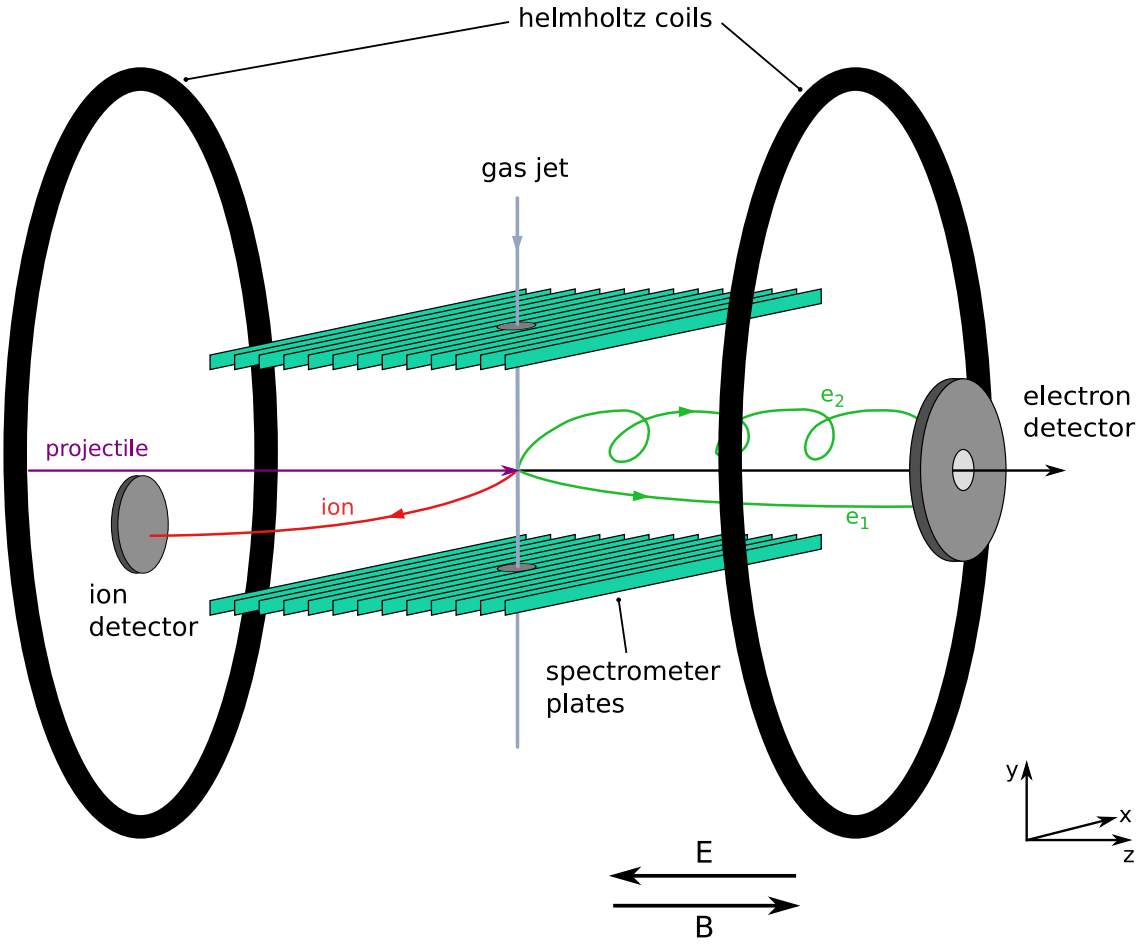

Figure 3.1.: Reaction microscope

in addition. As one can see from figure 3.1, the electron detector has a hole in the center. This is needed to prevent unscattered electrons from hitting the detector and hereby saturating it. They occur, since overall the cross-sections are quite low, but it is desireable to have only a single reaction with every shot of the electron gun, to prevent *false coincidences*. On the other hand this hole combined with a particular magnetic field strength limits the minimum transversal momentum to a value larger than zero. This is due to the fact that the magnetic field and the velocity in the transversal direction determine the cyclotron radius.
For the ion detector it is sufficient to have a smaller MCP below the spectrometer axis, because the position mainly depends on the jet pressure and the spectrometer voltage. Since there is a multitude of reactions to be observed, this holds only for atomic targets or molecules, for which only one reaction channel (e.g. single ionization) is of interest. For reactions, where dissociation processes are to be observed, a

larger detector, similar to the electron detector is needed (e.g. [20]). In the following sections a short overview of the details of apparatus and technique will be given.

3.1.1. Detectors

To detect all charged fragments produced in an atomic collision and afterwards recover the complete information about the process, one has to know when and where a particle has hit the detector. Both has to be done with good resolution and furthermore, since a number of fragments can be created, the detector has to be capable to register several particles without a considerable dead time. A basic design of the detector consists of two parts: a MCP and a position sensitive device, which can either be a *delayline anode* (for electrons) or a *wedge-and-strip anode* (for ions). For the different fragments (i.e. electrons and ions) the demands of the detection system are different in a way that for the ion, usually only one particle per reaction has to be detected, whereas for the electrons, two or more particles impinge on the same detector within a short period of time. Furthermore, the ions have a much higher mass a thus much longer TOF, compared to the electrons. This means that particularly the detection of electrons is crucial, for they have to be resolved in time and position, within very short time intervals (e.g. ns). Additionally the electron detector has a central hole. As mentioned above, this is to prevent from saturation which would be caused by unscattered electrons hitting the MCP. Of course, this hole creates a lower limit for the transversal momentum of electrons to still hit the detector (see section 3.1.2).

Microchannel Plate

A MCP is in principle just a secondary electron multiplier of which a schematic view can be seen in figure 3.2. In order to obtain position information a multitude of small channels (10-100 μm diameter) are oriented in parallel. The time resolution is typically in the order of < 1 ns and the spacial resolution is limited only by the diameter of the channels and their spacing. In addition there is a potential difference between the front and the back (typ.1 kV) of the MCP so that every secondary electron will be accelerated through the channel resulting in a cascade of electrons. In this way the small current of a single electron or ion is amplified and finally measureable.

The individual channels are made of leaded glass with surface optimized for a small work function for electrons. Front and back side are covered with a metal substrate of low resistance. The amplification is of the order of 10^4 and can be increased by multiple layers of single MCPs. To reach a higher efficiency the channels of the individual MCPs form a slight angle with the channels of the next MCP. In this way the electrons are bound to hit the surfaces more often, since now, they cannot

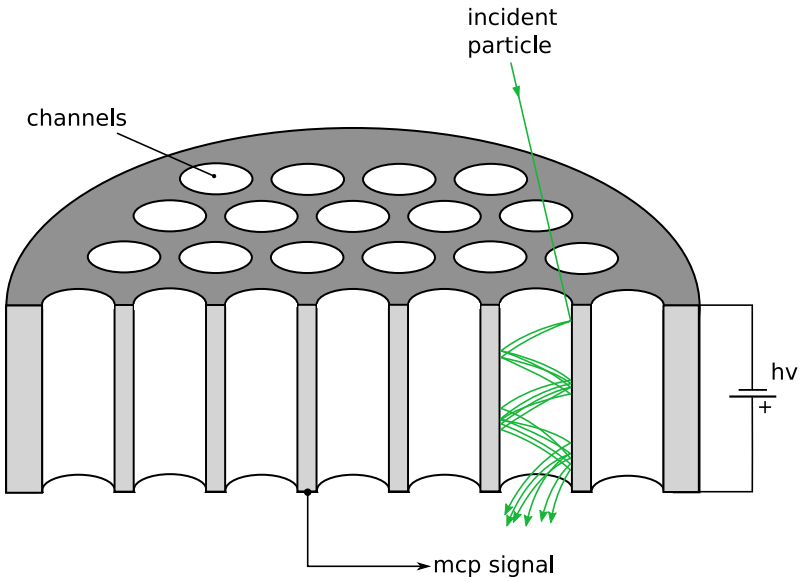

Figure 3.2.: scheme of a MCP

pass the stack by a straight line and therefore produce more emission electrons. Another advantage of tilted channels is the suppression of ion feedback which can be created by electrons ionizing residual gas or from desorption from the channel walls. The detection efficiency of an MCP can be assumed to be in the order of 50%.

Delayline Anode

While a MCP can be used to get a fast signal of a particle to measure the time of flight (TOF) while maintaining the information about the position the latter has to be reconstructed with good resolution. A common method for this kind of measurement is the use of a delayline anode. In its most simple form it consists of two perpendicular layers of wires. The wire of each layer is wound around an insulator as shown in figure 3.3. The principle by which position information is obtained is simply by measuring the time the induced charge needs to reach both ends of the wire. This is possible since fractions of the charge are traveling in both directions of the wire. The time between the MCP signal and the detection of charges at the respective wire ends results in the times t_{left} and t_{right}. While the total time – which is the sum of the individual times needed to reach the wire ends – is constant, the time difference at the ends is proportional to the position the charge cloud has hit the wire. The actual position x in one direction can then be calculated

$$x = v_{prop} \cdot ((t_{left} - t_0) - (t_{right} - t_0)) = v_{prop} \cdot (t_{left} - t_{right}) \tag{3.1}$$

where v_{prop} is the effective propagation velocity[1] for each direction and t_0 is the time the particles hit the MCP.
In order to improve the performance and reduce noise usually two wires for each direction are used. One serves as a *reference*-wire the other as the *signal*-wire. By biasing the two wires differently one can set the amount of charge traveling in each wire and in the following use a differential amplifier to analyze the difference of the two signals (i.e. *signal* and *reference*). First and foremost because of the small spacing all the noise will be induced in the same way in both wires and therefore cancel out by taking the signal difference.

As mentioned earlier the time sum of each layer is constant. This allows to sort

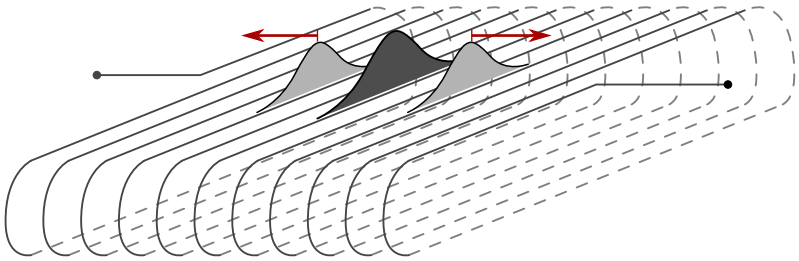

Figure 3.3.: delayline anode

out real events from noise by choosing only those which fulfill the condition

$$t_{sum} = (t_{left} - t_0) + (t_{right} - t_0) \stackrel{!}{=} const. \tag{3.2}$$

A problem arises when several particles hit the delayline within a short time and within a short distance. Then, because of overlapping delayline signals or the electronics dead time severe loss of position information is to be expected. Therefore the idea has come up to add a third layer to provide the redundance of reconstructing a particles position when the position information of on layer is lost.
While with only two layers the angle between them is 90°, with a three layers the angles between the layers are 60°. It is usually referred to as *hexanode* because of its resulting hexagonal structure. The new coordinates are named u,v and w so the

[1] The effective velocity the charge pulse travels perpendicular to the wire.

transformation back to x and y is as follows:

$$\begin{aligned} x_{uv} &= u \\ y_{uv} &= \frac{1}{\sqrt{3}} \cdot (u - 2v) \end{aligned}$$

$$\begin{aligned} x_{uw} &= u \\ y_{uw} &= -\frac{1}{\sqrt{3}} \cdot (u + 2w) \end{aligned}$$

$$\begin{aligned} x_{uv} &= (v - w) \\ y_{uv} &= -\frac{1}{\sqrt{3}} \cdot (u - w) \, . \end{aligned}$$

The reconstruction of the positions on the anode is by no means trivial and requires a sophisticated routine that can ensure to separate close hits from each other, as well as from background noise.

Wedge-and-strip Anode

For the position detection of the ions, a so called wedge-and-strip anode was used. Other than the delayline, described before, a wedge-and-strip anode has only very limited multi-hit capabilities since the amplified position signals normally have a duration of $\sim 1\,\mu$s. For detecting ions, however, this is not needed if no fragmentation processes are to be studied. The advantage of this type, on the other hand, is that no sophisticated read out system – usually consisting of differential amplifiers and discriminators – like for the delayline anode, is required (see 2.1). Figure 3.4 shows a scheme of the anode, where the three areas *wedge*, *strip* and *meander* can be seen.[2] They form individual electrodes. An ordinary detector would consist of an MCP for amplification purposes, where the enhanced charge cloud will deposit different amount of charges on the electrodes, depending on the hitting position. With the knowledge of the geometrical shape of these electrodes, one can reconstruct the center of gravity of the cloud.

This is possible since the area of the *wedge* changes in the y-direction, whereas the area of the *strip* changes in the x-direction. The purpose of the *meander* is to collect all charge neither hitting wedge nor strip, and thus being able to measure the total charge, impinging on the anode. The dependence of position and change can be expressed like

$$x \propto \frac{Q_s}{Q_{tot}} \qquad y \propto \frac{Q_w}{Q_{tot}} \, , \tag{3.3}$$

[2]Hence the name.

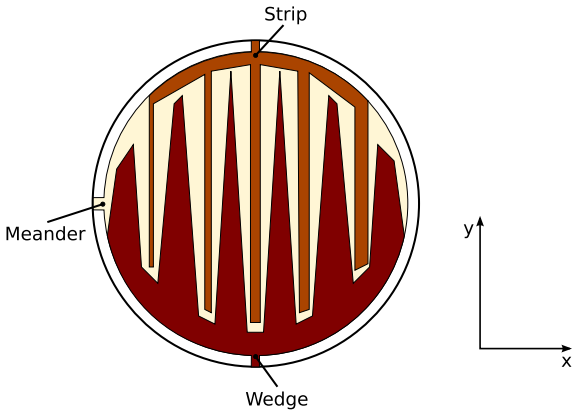

Figure 3.4.: Wedge-and-Strip anode.

where Q_w is the the charge fraction deposited on the wedge and Q_s on the strip. Q_{tot} is the charge sum of all three electrodes. In order to operate correctly, the charge cloud has to be sufficiently large in size compared to the anode structure, otherwise – as for the delayline anode – one resolves the individual structure of the anode and loses position information.

3.1.2. Spectrometer

In contrast to conventional methods in atomic or molecular collisions, where ordinarily only the electrons were detected, in a RM all charged fragments are detected at once. This is maintained over the whole solid angle of 4π. It is therefore possible to reconstruct all momenta directly. Since the electron detector has a hole in the middle with a radius of $\sim 5\,\mathrm{mm}$, this creates a minimum requirement for the transversal momentum.
While all the fragments are separated by charge sign with a homogeneous electric field, the electrons are then projected onto the detector by an additional magnetic field.[3] Since at least two electrons have to be detected for each collision, it is of great importance that the electron detector has very good multi-hit capabilities otherwise the distinction between the electrons would be impossible. Since the momenta of the electrons and the ions are of the same order, ions have a much lower velocity because of their higher mass. Therefore the magnetic field has a much lower impact compared to the electron. In that sense the ions are mainly influenced by the electric field and projected to a detector on the opposite direction of the electron's detector. The charged fragments first pass an acceleration length of $a = 11\,\mathrm{cm}$ and after that

[3]Normally in the order of a few Gauss

they pass a drift length of $d = 22\,\text{cm}$ until they impinge on their respective detectors. This geometry is symmetric for electrons and ions (see figure 3.1). The values of the drift length and the acceleration length are not independent of each other. Their specific connection is called *time focusing* [40], [30]. It accounts for the fact that the target jet has a finite extension in the xz-plane and therefore the *point of birth* of the charged fragments varies over the jet extension. One can then find - for a small initial momentum (i.e. $\mid p_{\text{II}} \mid \ll 1\,\text{a.u.}$) - a minimum for the TOF as a function of the acceleration length:

$$a = \frac{d}{2}\,. \tag{3.4}$$

The longitudinal momentum is then independent of the point where the reaction took place (see section A.1).
As mentioned before the electrons and the ions have comparable momenta but their velocities differ quite a lot. Therefore - if the spectrometer has been set up to image the ions - the fast electrons (e.g. scattered projectiles) can have a large transversal momentum, preventing them from hitting the detector. The magnetic field confines those electrons on a helicoid trajectory whose symmetricity is parallel to the spectrometer axis.[4] The reconstruction of the momenta is shown in section 3.2.2

3.1.3. Supersonic Gas Jet

As mentioned earlier the target consists of an atomic or molecular gas which expands into the chamber through a nozzle with a sufficiently high pressure. The result of such an expansion is the severe cooling of the target gas which is further improved by peeling off target constituents with high momentum components in the xz-plane – which is perpendicular to the jet – by so-called *skimmers* (see figure 3.5). After passing the nozzle the gas expands into an area with considerably lower pressure. The velocity of the jet is then higher than the local sound velocity, leading to an adiabatic expansion and since the entropy remains constant the temperature decreases. By applying this technique the jet can reach temperatures in the order of a few Kelvin leading to a very narrow energy distribution and therefore to an improved momentum resolution necessary for high-precision recoil momentum spectroscopy.
The first and second jet stage are separately pumped with pressures of $p_0 = 12\,\text{bar}$ before the nozzle, $p_1 = 4.1 \cdot 10^{-3}\,\text{mbar}$ in the first stage and a pressure in the second stage of $p_2 = 10^{-6}\,\text{mbar}$. The temperature of the target gas can be expressed by

$$T = T_0 \left(\frac{p}{p_0}\right)^{(\gamma-1)/\gamma}\,, \tag{3.5}$$

[4] As is the direction of the $\vec{B}$-field.

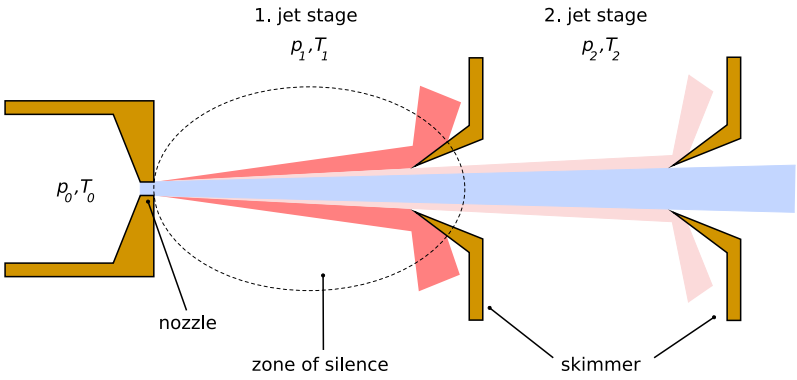

Figure 3.5.: target preparation with supersonic expansion and differential pumping stages. Shown in red are different fractions of the target gas with higher momenta perpendicular to the jet, which are peeled off by the skimmers.

where γ is the adiabatic coefficient and p is the pressure in the main chamber which was $\sim 10^{-8}$ mbar [29]. Starting from $T_0 = 300\,\mathrm{K}$, these values lead to a final jet temperature of $T \simeq 1.0\,\mathrm{K}$. Of course, the skimmer can't control the momentum spread in the direction of the jet. This is why the momentum resolution in this direction is usually worse than in the xz-plane.[5]
The nozzle has a diameter of $30\,\mu$m, while the first skimmer which is 2.2 mm away from the nozzle has a diameter of $200\,\mu$m. The second skimmer with a diameter of $400\,\mu$m is 19.7 mm away from the nozzle. After passing the second skimmer the remaining part of the target expands into the main chamber where the gas jet is crossed with a projectile beam. The xz-extension has then been collimated to a diameter of $\sim$ 1 mm FWHM which is acceptable since time-focusing has been applied, too (see section A.1).
By applying a high differential pressure between the nozzle and the main chamber the target gas can be partially condensed, thus forming clusters [8]. In this way, however, it is not possible to control the creation of a particular cluster size. The gas jet therefore contains clusters of various sizes. For typical temperatures of the jet one can assume that the target is in the vibrational ground state. Especially for clusters (or molecules in general) this is of great importance because within one electronic state the vibrational states are usually very close and therefore below the resolving power of the spectrometer. Having a cold target can ensure that the initial state is well defined.

[5] This could be improved by using a pulsed jet [1].

3.1.4. Data Acquisition

Normally for the electron detector the time and position signals are fed to a multi-hit Time-to-Digital Converter (TDC) whereas the ion detector signals are fed to an Amplitude-to-Digital Converter (ADC). Since the TOF for the argon dimer is by $\sqrt{2}$ longer than for the atom and since the TDC has a limited time range of 50 μs, a Time-to-Amplitude Converter (TAC) in combination with the ADC was be used to record the ion TOF.
In figure 3.6 one can see a scheme for the electron detector data acquisition.[6] The

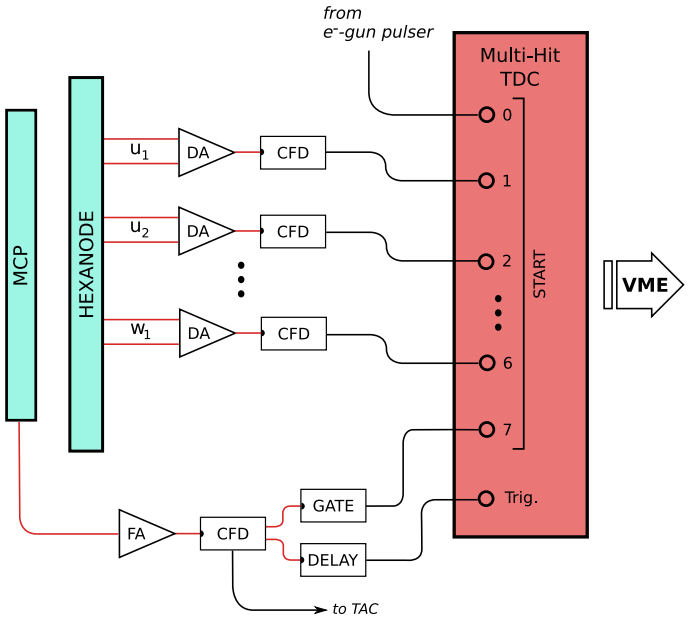

Figure 3.6.: scheme of the data acquisition for electrons

electrons impinging on the MCP produce a signal which is amplified by a fast amplifier (FA) and converted to a digital NIM pulse by a constant fraction discriminator (CFD). The CFD's output is then sent through a gate which can be set to a proper time range to minimize the effect of noise and false coincidences. Only those events which fulfill the gate's condition are sent to a channel of the multihit TDC. The same signal is also sent to a delay to trigger the TDC and to the TAC which is used to measure the ion TOF.
After the electron has set off an avalanche of secondary electrons, this charge cloud reaches the hexanode where the pulses on each individual layer are sent to Differential-Amplifiers (DA) and afterwards to CFD's. Those position signals are

[6]For clarity only the most important parts are shown.

fed directly to the TDC along with an additional signal of the electron pulser used to drive the electron gun, which is required for the time of flight measurement.
The TDC itself is used in Common-Stop-Mode, meaning that after it is triggered

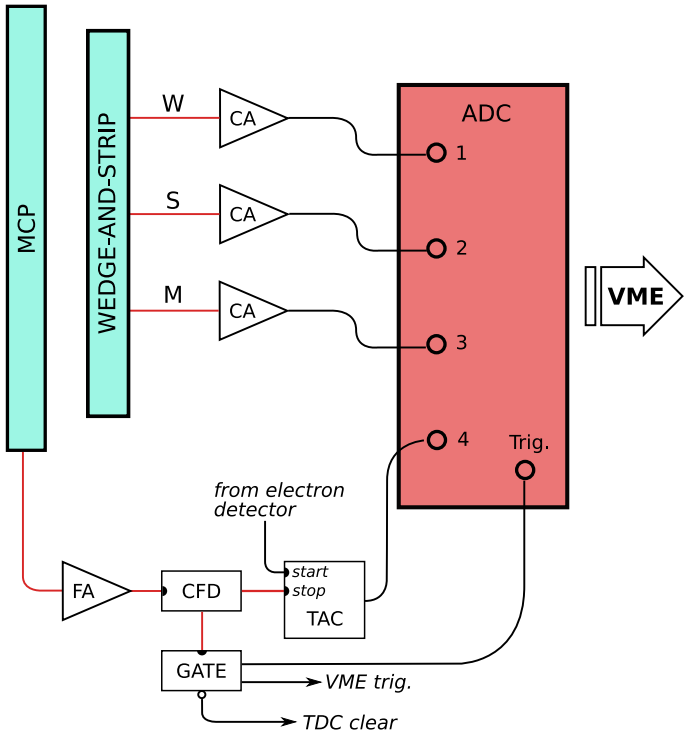

Figure 3.7.: scheme of the data acquisition for ions

it records the time back to the individual pulses. All the signals are now referenced by an arbitrary trigger whereas the real times are recovered by referencing them to the pulser signal. Ordinarily this setting is used to decide whether an event is good triggering by the ion.[7]
For the ion detector the position information is obtained not by a hexanode but by a so called wedge-and-strip detector as shown in section 3.1.1. It consists of three regions where the fraction of charge on each region can be used to reconstruct the position of the cloud. The tree signals are fed to charge amplifiers (CA) which - while maintaining low output impedance - deliver a voltage proportional to the charge at the input. These pulses are sent to an ADC.
The ion detector's MCP signal is also amplified and processed by a CFD and then sent - as a *stop* - to the TAC. The *start* is delivered by the electron detectors MCP

[7] an event is considered *good* only when an ion is detected

signal. The ion time of flight is now referenced to the fast electron and has therefore to be calibrated to a proper time. This is done by a comparison with a helium measurement where the time was measure with the TAC and the TDC simultaneously. Therefore for all spectrometer voltages helium was measured additionally under the same conditions and the TOF with the TAC was later calibrated to a real TOF. The ion's MCP signal is also sent to a gate which – if the preset TOF condition is fulfilled – triggers the ADC and the event processing computer (VME), which then acquires the data from both the TDC and the ADC. If the condition is not fulfilled a signal is sent to the TDC to clear its memory and the event will not be recorded.

3.2. Momentum Reconstruction

As mentioned earlier, with a reaction microscope the complete kinematic information of a given process can be derived. This is possible by measuring the TOF and the position of each charged particle on the respective detector. A relation between the time of flight and a particles longitudinal momentum can be derived simply by newton's equations of motion. Due to the geometry of the spectrometer the TOF of a particle with mass M and charge q is given by

$$t(p_{\shortparallel}) = M \cdot \left(\frac{2a}{\sqrt{p_{\shortparallel}^2 + 2MqU} + p_{\shortparallel}} + \frac{d}{\sqrt{p_{\shortparallel}^2 + 2MqU}} \right), \tag{3.6}$$

where a is the acceleration length, d is the drift length and $p_{\shortparallel}$ is the particles longitudinal momentum component.[8] It is, however, convenient to express the momentum components in cylindrical coordinates. The longitudinal momentum is then equal to p_z, while $p_\phi = \arctan(p_y/p_x) \equiv \phi$ and $p_r = \sqrt{p_x^2 + p_y^2}$ which will be denoted as $p_\perp$.[9]
As mentioned in section 3.1.2, the acceleration length and the drift length fulfill the condition $d = 2a$ in order to minimize the effect of the jets spacial extension in the z-direction (see section A.1). Of course, this solution has also a big advantage. Ordinarily, especially when low cross-sections are to be expected, one is in particular interested that the interaction volume can be enlarged, leading to a higher signal rate.

3.2.1. The Ion Momentum

Since even the lightest atom, hydrogen, has almost 2000 times the mass of an electron, the ions are much less influenced by the magnetic field. Furthermore, the initial longitudinal momentum is much lower than the momentum gained due to the

[8] in SI-units
[9] the z-axis is the direction of the projectile

spectrometer field. Lastly, since the electrons and ions have comparable momenta (i.e. $\sim O(1\,\text{a.u.})$), the velocity (and therefore the energy) of the ions are negligibly small, compared to the electrons. Eq. 3.6 can then be approximated by a Taylor expansion around $t(p_{\parallel} = 0)$. While neglecting higher-order terms, the expansion finally delivers

$$t(p_{\parallel})|_{p_{\parallel}=0} \;\simeq\; 2a\sqrt{\frac{2M}{qU}} + \frac{a}{qU}\cdot p_{\parallel} \;+\; O(p_{\parallel}^2)\;. \tag{3.7}$$

The inverse of equation 3.7 can now easily be found to be

$$p_{\parallel} = \frac{qU}{a}\cdot(\overbrace{t - \underbrace{2a\sqrt{\frac{2M}{qU}}}_{=:\,t(p_{\parallel}=0)}}^{=:\,\Delta t})\;, \tag{3.8}$$

which finally leads to

$$\boxed{p_{\parallel} = \frac{qU}{a}\cdot\Delta t}\;. \tag{3.9}$$

During the offline analysis $t(p_{\parallel} = 0)$ has to be determined (e.g. using the momentum sum and momentum conservation [15]).
In order to determine the transversal momentum $p_{\perp}$ of the recoil ion, its TOF and hitting position on the detector (i.e. x, y) are needed. Since the reaction is axially symmetric around the projectile beam, the center of the distribution (i.e. x_0, y_0) corresponds to ions with zero transversal momentum and the radial displacement is then connected to the momentum like

$$r := \sqrt{(x - x_0)^2 + (y - y_0)^2} = \frac{p_{\perp}}{M}\cdot t\;, \tag{3.10}$$

where t is the absolute TOF and the ejection angle is $\phi = \arctan[(y - y_0)/(x - x_0)]$. Since the change in the time of flight caused by the ion's initial longitudinal momentum is small compared to the absolute TOF (i.e. $\Delta t \ll t$), it is adequate to use $t(p_{\parallel} = 0)$ instead. This leads to

$$\boxed{p_{\perp} = \sqrt{\frac{MqU}{8}}\cdot\frac{r}{a}}\;. \tag{3.11}$$

3.2.2. The Electron Momentum

For better clarity figure 3.8(a) shows the coordinate system used in the following. The scattering plane (in red) is spanned by the projectiles initial and final momentum. All momenta are extracted by knowledge of the position on the detector and

the TOF.

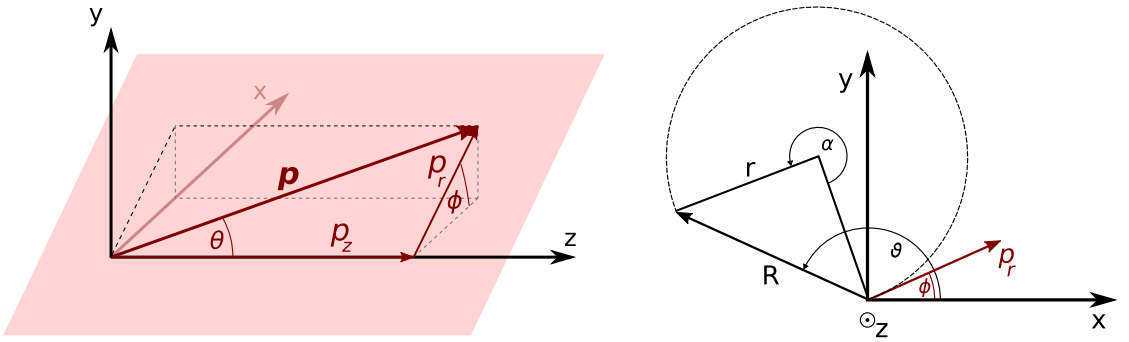

(a) momentum components (b) transverse momentum reconstruction

Figure 3.8.: Scattering geometry for the electrons

Longitudinal Momentum

From eq. 3.6 it can be seen that a particle's TOF is only dependent on its longitudinal momentum. Acquiring this component is then possible by solving this equation for $p_{\parallel}$. Although it is possible to receive an analytical solution it proves to be rather inconvenient to use it in the analysis. Instead it can be approximated by a simpler[10] function. First two substitutions are to be done

$$T := \frac{t_{TOF}\sqrt{eU}}{a\sqrt{2M_e}}, \qquad X^2 := \frac{p_{e\parallel}^2}{2M_e eU} . \tag{3.12}$$

With this eq. 3.6 can be written in a more concise form

$$T = \frac{1}{\sqrt{X^2+1}+X} + \frac{1}{\sqrt{X^2+1}} , \tag{3.13}$$

and the inverse can be approximated using

$$X = A + \frac{B}{T} + C \cdot T + D \cdot \sin(T) . \tag{3.14}$$

The four parameters are determined – by fitting this function – to be

$$A = -0.051 , \quad B = 1,508 , \quad C = -0.466 , \quad D = 0.2558 . \tag{3.15}$$

[10] And therefore faster to calculate.

For the longitudinal momentum of the electron one can write with eq. 3.12 and 3.14

$$\boxed{p_{e\parallel} = X \cdot \sqrt{2M_e eU}} \,. \tag{3.16}$$

Transversal Momentum

Because of the magnetic field applied in parallel to the spectrometer axis, the electrons are confined to a cyclotron motion as they travel to the detector. The frequency of revolutions is given by

$$\omega_c = \frac{eB}{M_e} \,, \tag{3.17}$$

and is only dependent on the magnetic field B. The radius of the cyclotron motion is – for a certain magnetic field – only dependent on the transversal momentum

$$r = \frac{p_{e\perp}}{eB} \,. \tag{3.18}$$

The complete situation is shown in figure 3.8(b), where the origin is the center of the electron detector and the dashed circle a projection of the trajectory. Instead of r, the observable is R and furthermore the electron can – in transversal direction – be ejected under an arbitrary angle ϕ. During the time the electron travels to the detector, the angle α between the startpoint and the endpoint along the xy-projection of the trajectory is $\alpha = \omega_c \cdot t_{TOF}$. For the connection between r and R one can then derive

$$r = \frac{R}{2|\sin(\frac{\alpha}{2})|} \equiv \frac{R}{2|\sin(\frac{\omega_c t_{TOF}}{2})|} \,, \tag{3.19}$$

and therefore with eq. 3.18

$$\boxed{p_{e\perp} = \frac{eRB}{2|\sin(\frac{\omega_c t_{TOF}}{2})|}} \,. \tag{3.20}$$

Finally the relation between the angle ϕ under which the electron has been emitted and the angle θ can be expressed as

$$\phi = \theta - \frac{\omega_c t_{TOF}}{2} \,. \tag{3.21}$$

3.2.3. Acceptance and Resolution

The acceptance of the spectrometer for the electrons is mainly limited by the size of the MCP and its hole in the middle. Furthermore, the radial extension of the electron trajectories is confined by a magnetic field. This restrains the detection of electrons to transversal momenta within a certain range. The radius of such a

helicoid trajectory is given by equation 3.18, which only depends on the magnetic field strength. The minimum (maximum) transversal momentum an electron has to have in order not to go through the hole in the detector (miss the detector) is given by half the radius of the the hole (of the MCP):

$$p_\perp|_{min,max} = \frac{r_{hole,dia}}{2} e\,B\ , \tag{3.22}$$

where the subscript *dia* stands for the diameter of the MCP (see figure 3.8(b)). For the given magnetic field of $B = 8.2\,\mathrm{G}$, this leads to values of $p_\perp|_{min} \simeq 0.17\,\mathrm{a.u.}$ ($\equiv 0.4\,\mathrm{eV}$) and $p_\perp|_{max} \simeq 1.31\,\mathrm{a.u.}$ ($\equiv 23.5\,\mathrm{eV}$). Secondly, because of the cyclotron motion, the time of flight and the cyclotron time (t_c) are connected in a way that if $t_{TOF} = n \cdot t_c\ \ , n \in \mathbb{N}$, all particles will return to the spectrometer axis, independent of their transversal momentum. This creates the so-called *wiggle* structure, shown in figure 3.9. Whenever this condition is met, the momentum information is lost. To recover theses gaps, the experiment for a single target species is done with three different spectrometer voltages, thus shifting those electrons to other parts of the *wiggles*. These three, in principle independent measurements, have to be combined during the offline analysis, meaning, to fill the empty regions in figure 3.10(a) by those of figure 3.10(b). The combination has to be done with great care, since not only have the edges of each wiggle to be cut, but also one has to take into account possible differences in the count rate. This requires the individual measurements to be scaled, to ensure a smooth transition. In this experiment the spectrometer voltages used where 15 V, 18 V and 23 V, the magnetic field was $B = 8.2\,\mathrm{G}$. The ions, on the other hand are much less influenced by the magnetic field. On the plus side, the wiggle structure has the advantage that one can directly determine t_c, the cyclotron time, which is important to reconstruct the time the reaction took place (see section 3.1.4). The reaction itself has to have taken place in such a gap since the the particles initially started on the spectrometer axis. So from this particular time to another gap in the spectrum 3.9 must lie an integer number of wiggles.

In general, the momentum resolution of the experiment is limited by the preparation of the target and the projectiles. In terms of the projectile it is important, how well-defined the energy is (i.e. monoenergetic) and how narrow the pulses can be. For the target – which is created by supersonic expansion – it is of importance, how good the thermal momentum of the gas before the expansion can be converted to a directed movement (see section 3.1.3). Of course, the detection of the fragments is not possible with perfect accuracy, so this subsequently limits the resolution further. In the supersonic expansion , the conversion of the thermal momentum of a target constituent to a directed movement leads to a momentum

$$p_{therm} = \sqrt{f k_B T_0 M}\ , \tag{3.23}$$

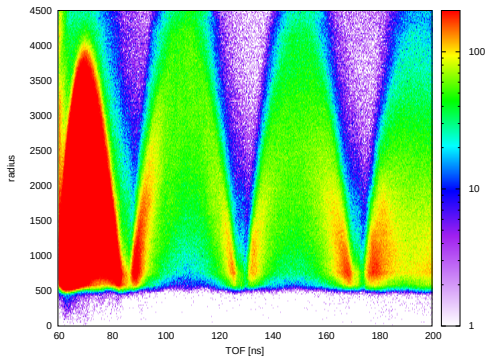

Figure 3.9.: Typical *wiggle* structure in the TOF vs. radius plot for electrons.

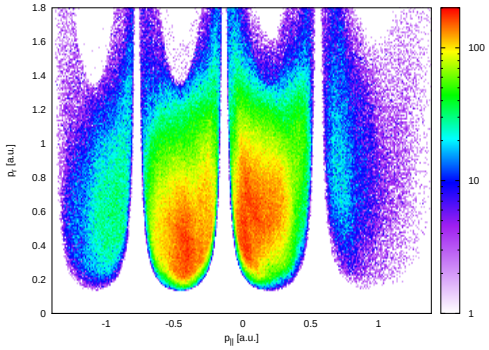

(a) 23 V

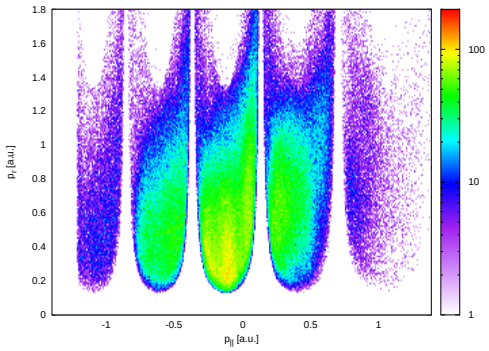

(b) 18 V

Figure 3.10.: Momentum space of the ejected electron for $U = 23\,\mathrm{V}$ and $U = 18\,\mathrm{V}$ spectrometer voltage. One can see the different intensity for the two voltages, as well as the decreased intensity at the edges of the wiggles.

	15 V	18 V	23 V
Δp_x	0.75 a.u.	0.78 a.u.	0.87 a.u.
Δp_y	1.42 a.u.	1.45 a.u.	1.50 a.u.
Δp_z	0.33 a.u.	0.33 a.u.	0.33 a.u.

Table 3.1.: Calculated precision of the momentum components for Ar^+ at different spectrometer voltages.

where M is the mass, T_0 the initial temperature of the gas, prior to the expansion and f, the degrees of freedom. At room temperature, this leads to $p = 14.43$ a.u. for Ar. However, the gas constituents do not move in parallel after the expansion, but radial starting from the nozzle (see figure 3.5). For that reason and the fact, that internal collisions occur due to the finite temperature, the initial momentum is not known exactly. The momentum uncertainty in the jet direction – derived from eq. 3.23 for a remaining temperature of 1 K – is $\Delta p_y \approx 1.27$ a.u.. The skimmers, which have been installed, limit the momentum components in the xz-plane – due to their position and size – to an uncertainty of $\Delta p_{xz} \approx 0.33$ a.u. in the perpendicular direction. For argon dimers and larger argon clusters, the uncertainty scales with $\sqrt{M}$, leading to a larger momentum spread and a reduced resolution.[11]
For the total resolution, one has to take the precision of the time and position measurement into account. The precision of the time measurement is assumed to be 1.5 ns resulting from the pulse width of the electron beam, whereas for the position measurement 1 mm is assumed, which is approximately the beam diameter. The final precision is dependent on the spectrometer voltage and can be seen for atomic argon, in table 3.1. Again, for Ar_n the precision in of the transversal momentum components scale with $\sqrt{n}$, while – for the ions – the longitudinal momentum is independent of the mass (see section 3.2.1).

The momenta of the electrons, gained in the experiment, are much larger than those, resulting from their thermal energy. Therefore, the resolution for the electrons depends mainly on the time and position measurement and the uncertainty for the respective momenta can be obtained through equations 3.20 and 3.16:

[11] Also one must consider the number of degrees of freedom.

$$\delta p_{e\perp} = \frac{eB}{2|\sin(\frac{\omega_c t_{TOF}}{2})|}\sqrt{\delta R_e^2 + \left(\frac{R_e\,\omega_c\,\delta t_{TOF}}{2\tan(\frac{\omega_c t_{TOF}}{2})}\right)^2} \tag{3.24}$$

$$\delta\phi_e = \sqrt{\left(\frac{\delta R_e}{R_e}\right)^2 + \left(\frac{\omega_c}{2}\,\delta t_{TOF}\right)^2}, \tag{3.25}$$

$$\delta p_{e\parallel} = \sqrt{\frac{eU}{2m_e}}\left(-\frac{B}{\frac{t_{TOF}{}^2}{a}\frac{eU}{2m_e}} + \frac{C}{a} + \frac{D}{a}\cos\left(\frac{t_{TOF}}{a}\sqrt{\frac{eU}{2m_e}}\right)\right)\delta t_{TOF} \tag{3.26}$$

where B is the magnetic field strength, ω_c the cyclotron frequency and R the distance of the electron, measured from the center of the detector (see section 3.2). As one can see, the longitudinal momentum resolution depends only on the TOF whereas the resolution of the transversal component and the ejection angle ϕ additionally depend on the position on the detector. Also, in the transversal direction, the resolution behaves periodical.

3.3. Measurement Procedure

It has been mentioned in section 3.2.3 that in order to recover the momentum information which was lost due to the wiggle structure, the experiment had to be performed for three different spectrometer voltages for each target. To ensure comparability of the results between Ar and Ar_2, the experiment was carried out, one spectrometer voltage at a time for all targets before switching to the next voltage. This was done to assure that for a particular setting, all targets are measured within a comparatively short period of time. Since especially for argon dimers the count rate was low, the overall measuring for a specific voltage was between two to three weeks. Measuring all targets for on voltage prohibited the effect of possible long term drifts (e.g. the quality of the cathode or the magnetic field) to be apparent only for one target.

4. Results

The present experiment was carried out, focusing on two main goals: The single ionization of Ar_2 and the comparison to single ionization of Ar by electron impact in a kinematically complete experiment at 100 eV projectile energy. Since the binding energies in van-der-Waals molecules are weak, the question arises, whether in a simple complex like Ar_2 mechanisms for single ionization are different compared to individual atoms and therefore if Ar_2 is a real molecule or merely two argon atoms nearby. Furthermore, for the ionization of larger argon clusters – such as Ar_3 or Ar_4 – differential data could be obtained.
For the non-dissociative ionization of Ar_2 it was possible to acquire triply differential cross-sections (TDCS). It was also possible to compare the FDCS for argon dimers and atoms, giving first hints of a real difference in the ionization process. For larger clusters, only lower orders of differential cross-sections could be obtained, due to the low count rate. Nevertheless, the energy loss spectra of argon and larger clusters indicate additional features. In both cases a second line was found, resulting from a simultaneous ionization/excitation process.

4.1. Single Ionization of Argon

For argon a kinematically complete experiment at 100 eV projectile energy was performed, where fully differential cross-sections could be obtained. In figure 4.1(a) the *energy sum* or energy loss spectrum is presented. Plotted is the number of counts as a function of the sum energy of the scattered projectile and the ejected electron. Since the energy of the ion can be neglected, the energy conservation reads $E_0 - IP = E_1 + E_2$. E_0 is the initial energy of the projectile, while $E_{1,2}$ are the energies of the scattered projectile and the ejected electron, respectively. The variable IP on the left hand side stands for the internal energy converted in the reaction. In general it is just the ionization potential, but can contain additional energy needed to excite the ion. In that sense, the energies in figure 4.1 are equal to the energy loss of the projectile. The peak at (84.37 ± 0.02) eV corresponds to the direct ionization of a $3p$-electron. As mentioned before, whether the ion is in a $^2P_{1/2}$ or $^2P_{3/2}$ state could not be resolved. On the other hand, a second contribution to the spectrum at (63.14 ± 0.45) eV could be distinguished, although having a quite low intensity. In previous experiments with higher projectile energies (i.e. 200 eV), this second peak

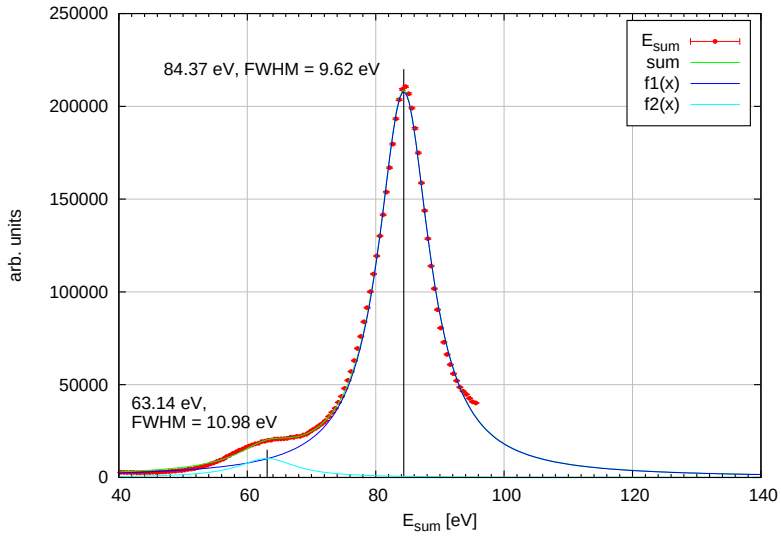

(a) Energy sum spectrum for single ionization of Ar at 100 eV projectile energy.

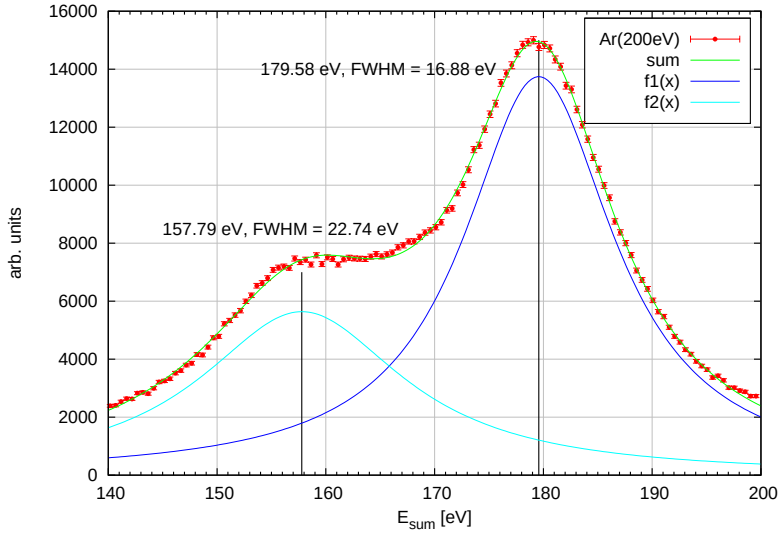

(b) Energy sum spectrum for single ionization of Ar at 200 eV (●). The relative difference of the peaks is 21 eV.

Figure 4.1.: Sum of the scattered projectiles (e_1) and the ejected electrons (e_2) energy for single ionization of Ar at 100 eV and 200 eV projectile energy. Both show a second feature 21 eV appart from the main line. The fits have been done using Lorentz functions.

was also apparent, but with an increased intensity (see figure 4.1(b)). Nevertheless, the performed fit could be carried out with the same quality. The difference in intensity is not believed to be of physical nature, but due to the acceptance of the setup at different experimental conditions (e.g. different magnetic field). This second feature is applicable for a ionization/excitation process, where the atom is ionized by ejecting one $3p$ - electron to the continuum and simultaneously exciting another $3p$ - electron to a state 21 eV above the Ar^+ ground state. The width of the main line was determined to be (9.62 ± 0.06) eV (FWHM), whereas the second line's was (10.98 ± 0.7) eV (FWHM). The second line's intensity is 5% of the main line intensity. Since the limitation in the energy resolution in the order of ~ 10 eV, it cannot be considered to be only a particular state to be populated, but a number of states, although the fit could be performed by using only two functions. This argument is enhanced by the fact that the width of the second line is larger than the width of the first line whereas the resolution improves for lower energy. The larger width can therefore be directly accounted to the excitation to different levels. As mentioned in section 2.1, there is a considerable number of possible excited states around 21 eV above the ground state of Ar^+, and almost all excitation cross-sections for those states peak at 100 eV. However, it is surprising, that there is no indication of a possible $3s3p^6$ contribution at this energy and a second order ionization/excitation process, seems much more likely, than the ejection of a $3s$ - electron. For electron impact, it has been shown experimentaly that particularly the excitation cross-sections with an electron in the $3d'$ or the $4d$ orbital are by far higher then those of lower states [38]. In the same publication, the authors where puzzled by especially high cross-section of the $4d$ - states and accounted it to possible configuration-interaction effects with the $3d$ - states. Still, the highest cross-sections for the $3d'$ - states found, are in the order of $15 \cdot 10^{-19}\,\mathrm{cm}^2$, while for $4d\ ^2D_{3/2}$ it is $157.5 \cdot 10^{-19}\,\mathrm{cm}^2$. It can therefore be expected that the contribution at 63.14 eV, in figure 4.1(a), is mainly due to a combination of $3d'$ and $4d$ - states.

The obtained fully differential data are compared with theoretical calculations done in first and second order born R-matrix approximation (see figure 4.3 and 4.2).[1] In the lower energy regime this approximation is known to underestimate the recoil peak and the post collision interaction. This is due to the fact that this approximation doesn't contain interaction between the scattered projectile and the ejected electron in the final state. It leads to a stronger enhancement of the calculated data in the forward direction (i.e. projectile direction), where the Coulomb repulsion between the two electrons is suppressing the cross-section.

Since the experimental data are not on an absolute scale they had to be normalized in order to be comparable to the calculations. This was done by scaling the datapoints to the intensity of the 2nd Born binary peak in the coplanar geometry. By looking at figure 4.2, one can see that generally the position of the maxima and min-

[1] The calculations where done by K. Bartschat.

ima can be reproduced by this theory at least in the coplanar plane. The intensity ratio between the binary and the recoil peak is better reproduced by the more sophisticated second order theory. In the perpendicular plane the agreement is not so good. One can see in figure 4.2(a) that the cross-section increases towards the backward direction (i.e. against the direction of the incoming projectile) and that the data shows two peaks at 120 and 240 degrees, respectively. However, there appears to be another structure at 85 and 275 degrees. For the 2nd approximation, there are two peaks visible at 140 and 220 degrees, respectively and a strong enhancement towards the backward direction. The same structure is also apparent in figure 4.3(a) for smaller scattering angle of the projectile and smaller momentum transfer, with the difference that the peaks are more pronounced. The calculation shows the same relative intensity. The experimental data, however, shows a significant difference in intensity. In all cases the second order calculation is in slightly better agreement with the experiment than the first order calculation. This indicates – as it was discussed before in section 2.1 – that higher order scattering processes, where the projectile scatters on the ionic potential or other electrons, are responsible for the high cross-sections in the perpendicular plane.
A characteristic feature in the ionization of argon – which has been discussed in section 2.1.1 – can be seen in the binary peak. Below $\sim 60\,^\circ$ there appears a minimum, which is also apparent in the calculation. It originates from the fact that the ionized electron is a p-electron and its momentum wave function is zero for zero momentum.

In figure 4.4 one can see another advantage of the applied reaction microscope technique. Since during the measurement all events over the whole solid angle are detected it is possible to reconstruct a 3D image of the cross-section. Figure 4.4(a) shows a particular example for a scattering angle of the projectile of $\theta_{e1} = -15 \pm 4\,^\circ$ and an energy for the ejected electron of $E_{e2} = 10 \pm 4\,\mathrm{eV}$, while in figure 4.4(b) a 2nd Born R-Matrix calculation for the same kinematic variables is shown. The direction of the projectile is upwards. Again, the characteristic lobe structure is visible where bigger one corresponds to the binary peak and the smaller one to the recoil peak. The cross-section in figure 4.2(a) is simply the slice of figure 4.4(a) containing the momentum transfer $\vec{q}$, the scattered projectile momentum $\vec{p}_{e1}$ and the initial projectile momentum $\vec{p}_{e0}$. In comparison with the theory one can see what the 2D data in figure 4.2(a) already indicated: The position of the lobes is reproduced quite well whereas the structure isn't.

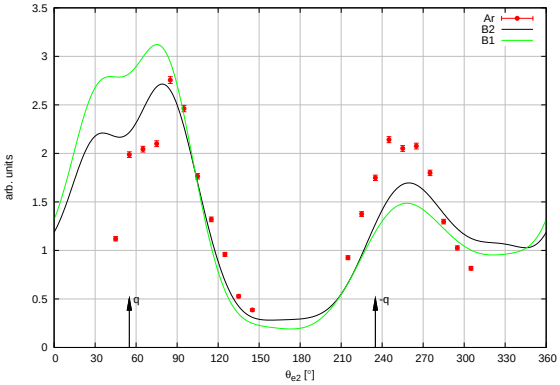

(a) Scattering plane: Binary peak along the momentum transfer direction $\vec{q}$ at 50°. Recoil peak along $-\vec{q}$ at 250°. Binary peak structure is due to the $3p$ bound state momentum wave function.

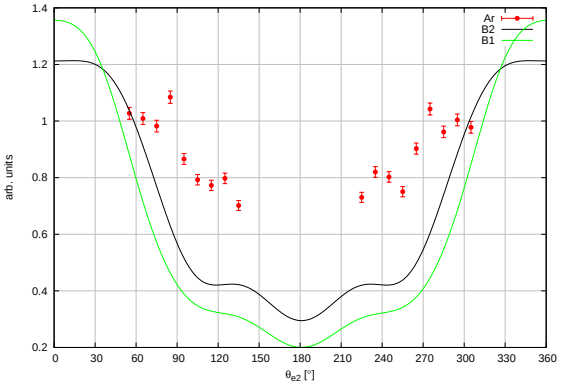

(b) Perpendicular plane.

Figure 4.2.: FDCS for $\theta_{e1} = -15 \pm 4°$ and $E_{e2} = 10 \pm 4\,eV$. Shown in solid curves are the 2nd Born (–) and the 1st Born (–) approximation.

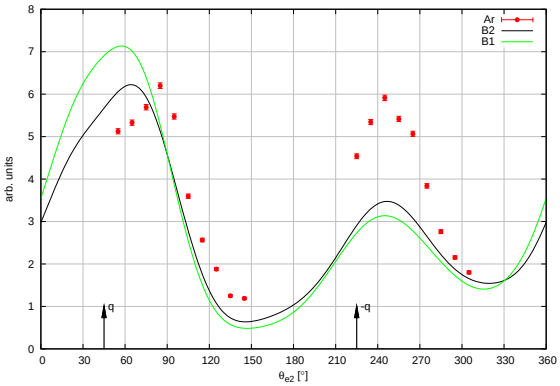

(a) Scattering plane.

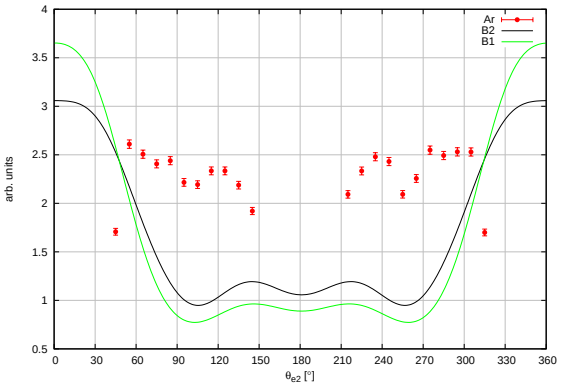

(b) Perpendicular plane.

Figure 4.3.: FDCS for $\theta_{e1} = -10 \pm 4°$ and $E_{e2} = 10 \pm 4\,eV$. Shown in solid curves are the 2nd Born (–) and the 1st Born (–) approximation.

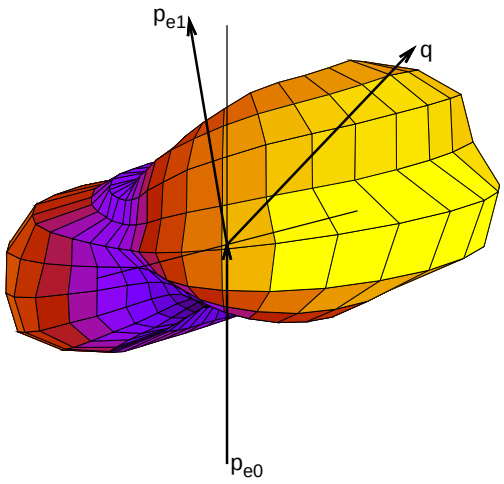

(a) Experimental data

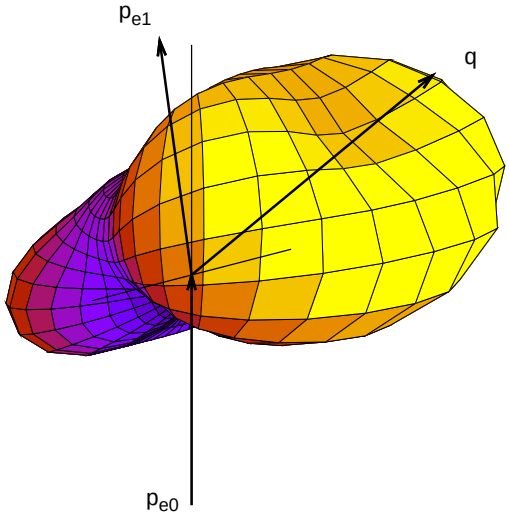

(b) 2nd Born R-Matrix calculation

Figure 4.4.: 3D images of the FDCS for Ar at a scattering angle of the projectile $\theta_{e1} = -15 \pm 4°$ and an energy of the ejected electron $E_{e2} = 10 \pm 4\,eV$.

4.2. Single Ionization of Argon Dimers

For the noble gas dimer Ar_2, fully differential cross-sections could also be obtained. Since the experiment was carried out under identical conditions as for Ar, a direct comparison is possible. Sadly, no theoretical calculations are available so far to further compare the data.
As already shown in section 4.1, figure 4.5 shows an energy sum plot for the single ionization of Ar_2. Apparently, there is no indication of any simultaneous ionization/excitation process like in Ar, leading to a stable Ar_2^{+*}. This could be due to the fact that there doesn't exist a bound state for higher excited Ar_2^{+*}. After all, the states accessible from the ground state, as shown in figure 2.3, are very close to the dissociation limit. Since there are presently no calculations of potential surfaces for energies $\sim 13\,\text{eV}$ above the Ar_2^+ groundstate, this point remains speculative. However, if argon dimers are thought of as two single argon atoms, there should be no reason, why a simultaneous ionization/excitation should not be possible. The fit was performed in the same manner as the previous ones and leads to a position of the peak at $(84.75 \pm 0.02)\,\text{eV}$ and a width of $(9.90 \pm 0.07)\,\text{eV}$ (FWHM).

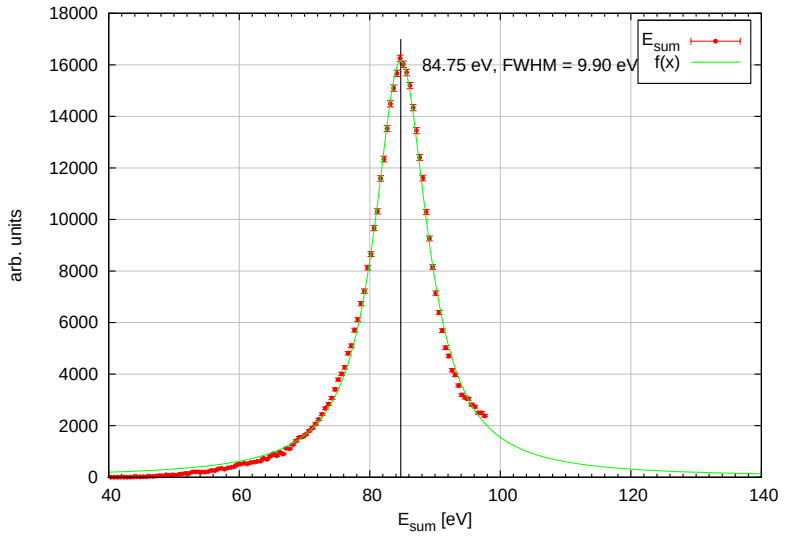

Figure 4.5.: Energy sum spectrum for single ionization of Ar_2 at 100 eV projectile energy.

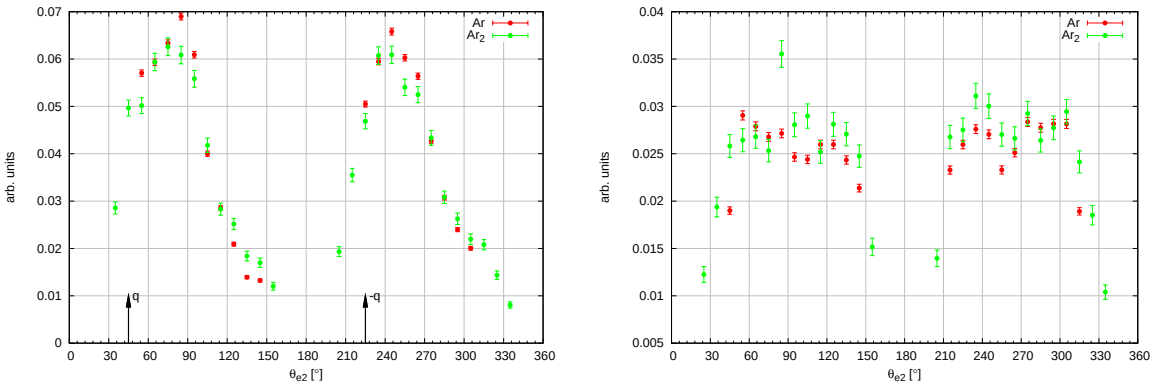

(a) Scattering plane.

(b) Perpendicular plane.

Figure 4.6.: FDCS for $\theta_{e1} = -10 \pm 4°$ and $E_{e2} = 10 \pm 4\,eV$. The green datapoints correspond to Ar_2, whereas the red points to Ar.

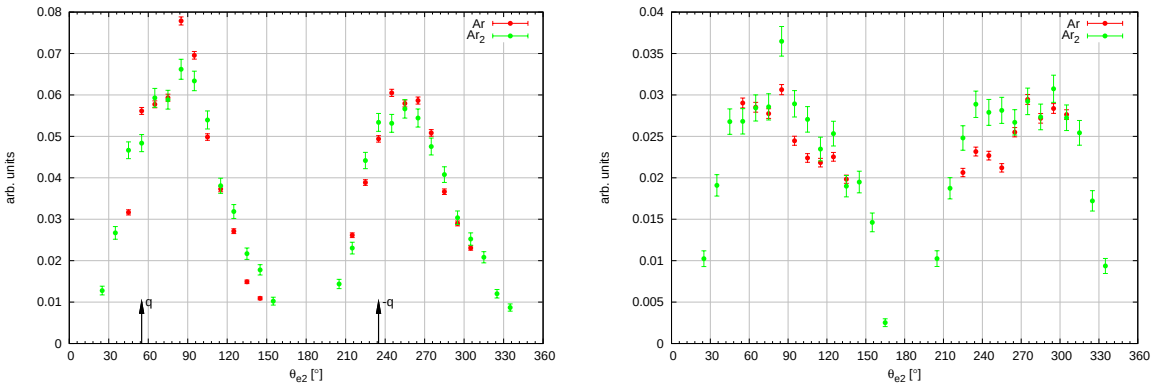

(a) Scattering plane.

(b) Perpendicular plane.

Figure 4.7.: FDCS for $\theta_{e1} = -15 \pm 4°$ and $E_{e2} = 10 \pm 4\,eV$. The green datapoints correspond to Ar_2, whereas the red points to Ar.

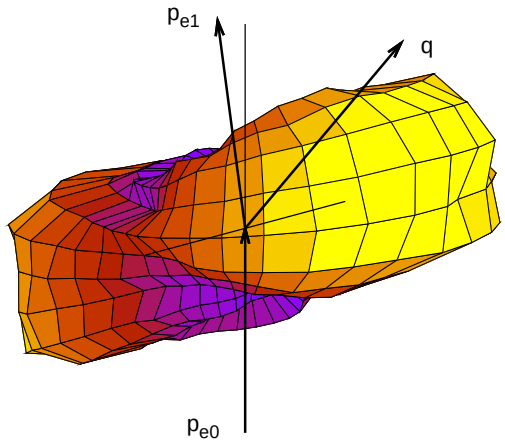

(a) FDCS for $\theta_{e1} = -10 \pm 4°$ and $E_{e2} = 10 \pm 4\,eV$.

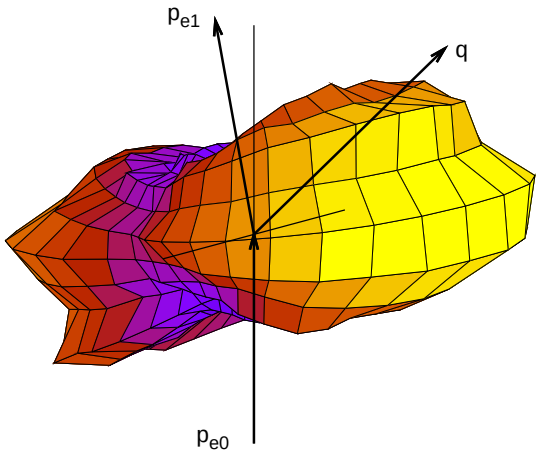

(b) FDCS for $\theta_{e1} = -15 \pm 4°$ and $E_{e2} = 10 \pm 4\,eV$.

Figure 4.8.: 3D images of the FDCS for single ionization of Ar_2 at different kinematic settings. Denoted with $\vec{q}$ is the momentum transfer, while $\vec{p}_{e0,e1}$ illustrates the projectile and the scattered projectile, respectively.

4.2.1. Triply Differential Data

In figures 4.6 and 4.7 one can see a combined plot of the TDCS for Ar and Ar_2. To make them comparable, each dataset for the coplanar geometry was normalized to its integral value.[2] The respective perpendicular data was scaled with the same factors, hence the differences in the cross-sections are absolute. The plots shown correspond to an energy of the ejected electron of $E_{e2} = 10\,\mathrm{eV}$, where 4.6 corresponds to a scattering angle of $\theta_{e1} = 10\,^\circ$, while 4.7 corresponds to a scattering angle of $\theta_{e1} = 15\,^\circ$. It is conspicuous that for the two ejection angles the coplanar data does not differ dramatically, whereas in the perpendicular plane one can see a difference in shape and intensity. Interestingly, there seems to be a higher probability in the case of the dimer for the second electron, to be ejected into this plane.
Overall it can be seen that the enhancement in the perpendicular plane is large preferably in the backwards direction. One can also see that this enhancement increases with the projectile scattering angle θ_{e1}. A possible reason for this enhanced *out-of-plane* cross-section is that for either the ejected electron or the scattered projectile, an additional elastic scattering process is involved. In [12] it has been shown that the total elastic cross-section increases with lower energy, and that for Ar, the DCS has two distinct minima at $\sim 50\,^\circ$ and $\sim 130\,^\circ$ for energies in the range of $\sim 30 - 100\,\mathrm{eV}$. At $\sim 100\,^\circ$ the distribution has a broad maximum with an intensity in the order of $\sim 10\,\mathrm{a}_0^2$ (see figure 4.9). Indeed, if the ejected electron would be involved in an elastic scattering process, it would be isotropically scattered to any plane between the scattering plane and the perpendicular plane. On the other hand, the intensity in the coplanar plane is much higher (i.e. the cross-section is larger) than for the perpendicular plane. Therefore, one could argue that a small change in intensity would be more likely to be observed in the perpendicular plane. In figure 4.8 a 3D plot for the FDCS can be seen. The plots correspond to a scattering angle of the projectile $\theta_{e1} = -10 \pm 4\,^\circ$ for figure 4.8(a) and $\theta_{e1} = -15 \pm 4\,^\circ$ for figure 4.8(b) while both plots are done for an energy of the ejected electron of $E_{e2} = 10 \pm 4\,\mathrm{eV}$.

4.2.2. Angular Distribution of the Scattered Projectile

As a second comparison between atomic argon and argon dimers, the angular distribution of the scattered projectile has been studied. In a first step the distribution has been integrated over all angles θ_{e2} and energies E_{e2} of the ejected electron. As shown in figure 4.10(a), the dimer's cross-section starts for small angles below the atom's, intersects at $\theta_{e2} = 14°$ for a first time, and at $\theta_{e2} = 28°$ for a second time. Since both distributions decrease towards higher energies, the cross-section ratio (i.e. $\mathrm{d}\sigma_{Ar}/\mathrm{d}\sigma_{Ar_2}$), plotted in figure 4.10(b), shows only their deviation. One can see

[2] Which can be seen as normalization with respect to the different measuring time and target density.

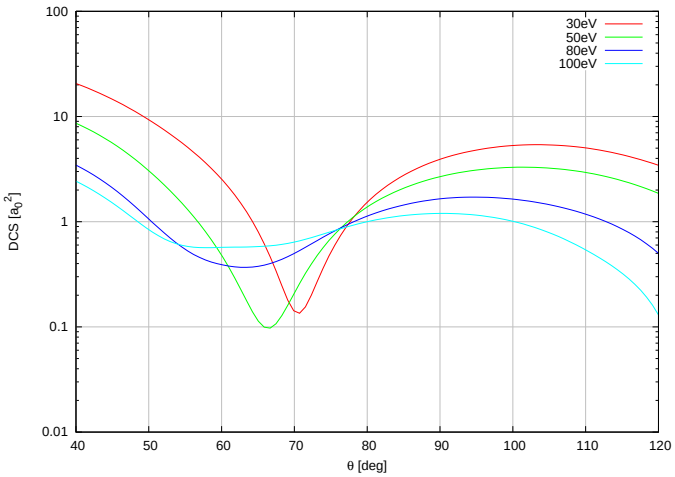

Figure 4.9.: Differential cross-section for elastic electron scattering on argon for different energies [12].

a distinct minimum at $\theta_{e2} = 23°$.

It has been mentioned in section 2.2.2 that interference in diatomic molecules has been predicted, and that, for unaligned molecules, interference should still be apparent. Therefore, also plotted in figure 4.10(b) is equation 2.7, using the appropriate value for the intermolecular distance of $R = 7.1$ a.u.. As on can see, the minimum of the interference pattern at 24 degrees can be reproduced quite nicely. The maximum at lower angles, however, shows some discrepancy. One should note that the ejection angle has not been fixed, due to the limited count rate. For comparison, figure 4.11(b) shows the energy distributions of the ejected electrons. As one can see, the two curves intersect at ~ 10 eV. For the ionization of Ar_2 this means a reduced amount of electrons with energies below 10 eV compared to atomic argon and an increased amount for energies larger than 10 eV. Qualitatively, this could be understood by looking at equation 2.7. If the sine-function is zero, there should be no difference between the two cross-section. However, if the sine-function is negative, the molecular cross-section is reduced. Since the internuclear distance for the dimer is given in table 2.1 with 3.762 Å ($\equiv 7.1$ a.u.), a full sinusoidal oscillation would cover electron momenta of $p_{e2} = 0 \ldots 0.88$ a.u., which is equivalent to energies of $E_{e2} = 0 \ldots 10.62$ eV. This means, since at an energy $E_{e2} = 10.62$ eV, the argument of the sine function is 2π, for electrons ejected with a smaller momentum, the cross-section should be reduced or enhanced for a higher momentum. Secondly, it should be mentioned that the energy for electrons with the de Broglie wavelength of $\lambda_B = 3.762$ Å or 7.2 a.u. is 10.62 eV. This, of course, comes from the fact that in atomic units $\vec{p} \equiv \vec{k}$. Since $|\vec{k}| = 2\pi/\lambda_B$, one would expect the sine function in eq.

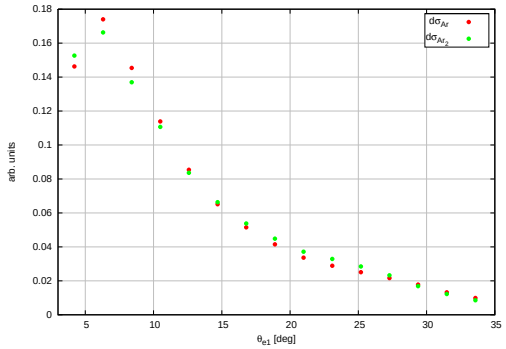

(a) Angular distribution.

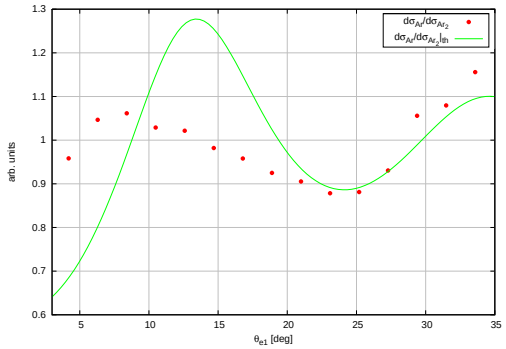

(b) Angular distribution ratio.

Figure 4.10.: Angular distribution for Ar (●) and Ar_2 (●) with energies for the ejected electron of $E_{e2} = 0 \ldots 5\,\mathrm{eV}$. The data has been normalized to their integral values, respectively.

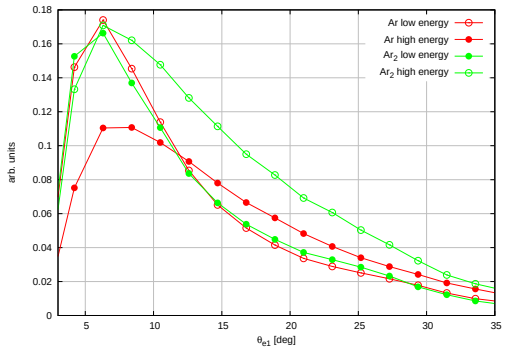

(a) Angular distribution for Ar and Ar_2 compared for energies $E_{e2} = 0 \ldots 5\,\mathrm{eV}$ and $E_{e2} = 12 \ldots 20\,\mathrm{eV}$. The high energy data has been scaled with the respective low energy integral value.

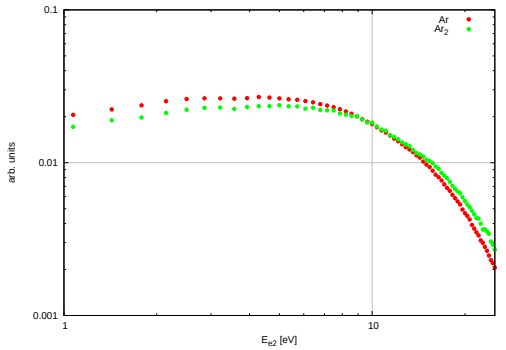

(b) Energy distribution of the ejected electron for Ar (●) and Ar_2 (●).

Figure 4.11.: Compared angular distributions for Ar and Ar_2 with energies for the ejected electron of $E_{e2} = 0 \ldots 5\,\mathrm{eV}$ and $E_{e2} = 12 \ldots 20\,\mathrm{eV}$. The data has been normalized to their respective integral value. Also shown are the energy distributions of the ejected electron.

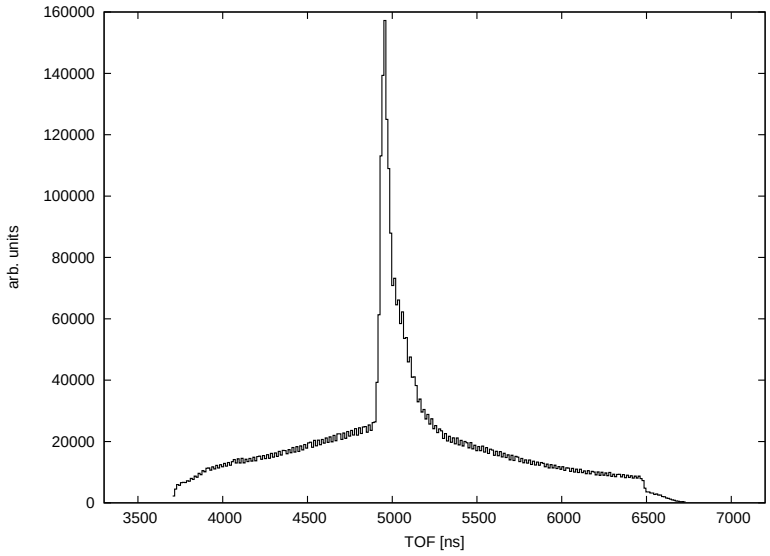

Figure 4.12.: TOF signal for Ar_2^+.

2.7 to be zero for $\lambda_B = R$.
Another interesting feature was discovered by restricting the energy of the ejected electron to certain ranges (i.e. $E_{e2} = 0 \ldots 5\,\text{eV}$ and $E_{e2} = 12 \ldots 20\,\text{eV}$). By looking at figure 4.11(a), where the angular distribution of the scattered projectile θ_{e1} has been plotted, one can observe distinct differences between Ar and Ar_2. For Ar, a severely reduced number of counts for faster ejected electrons at low scattering angles, compared to Ar_2, where the intensity is comparable, has been observed (see figure 4.11(a)).

4.3. Ionization of Larger Clusters

In section 2.2.1, it was mentioned that at least Ar_3 and Ar_4 dissociate into Ar_2^+, if ionized. This behavior should be observable in the TOF spectrum of the dimer ions. If a neutral dimer gets ionized, it will hit the detector in a given time, depending on the magnitude of momentum gained in the collision and the direction of its ejection (i.e. in or against the direction of the detector). A TOF peak with a certain width is observed. For the dissociation of larger clusters into dimer ions, the additional momentum gained leads to a strong broadening of the TOF signal. In figure 4.12, the TOF signal for Ar_2^+ is shown and clearly, a sharp peak with broad shoulders is visible. By selecting only events, for which the ion TOF lies in those shoulders, one is able to study dimer ions, originating from dissociation of larger clusters, exclu-

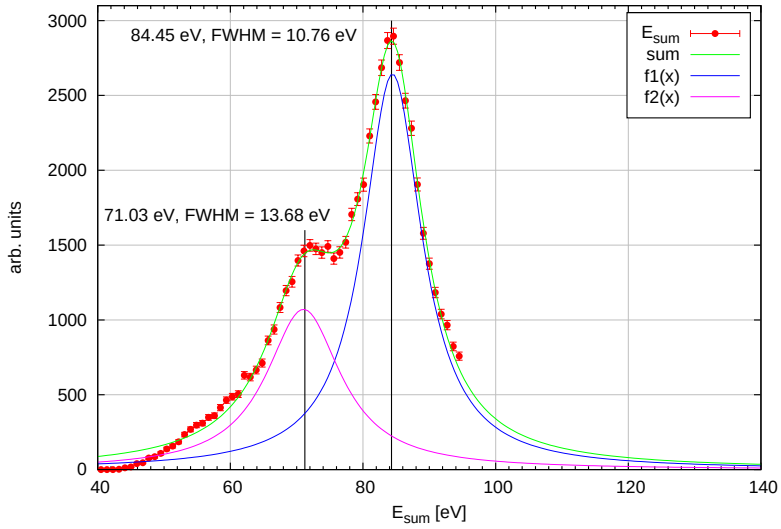

Figure 4.13.: Energy sum spectrum for the single ionization of Ar_n, $(n > 2)$.

sively.

The statistics (i.e. count rate), however, was insufficient for obtaining fully differential data. Nevertheless, by looking at the energy sum spectrum in figure 4.13, again, an interesting structure appears. The main line, located at (84.45 ± 0.07) eV and a width of (10.76 ± 0.25) eV (FWHM) refers to the single ionization of a larger cluster, like Ar_3 or Ar_4 since those have similar ionization potentials as argon itself.[3] The second line at (71.03 ± 0.22) eV with a width of (13.68 ± 0.62) eV refers – like for atomic argon, discussed in section 4.1 – to a simultaneous ionization/excitation process. For example, if Ar_3 is ionized it dissociates into $Ar_2^+ + Ar$ (see section 2.2.1), this neutral Ar could, of course, be excited for example to $3p^5(^2P_{3/2})4p$, which is 13.01 eV above the ground state, or any other of the remaining $4p$-states (see section A.2). From the fact, that the width of the second line is larger it can be argued that multiple states must contribute.

A comparison of the different intensity of the lines shows, that the second line's height is 40.5% of the first line at (84.37 ± 0.07) eV. Compared to the ionization/excitation process in atomic argon, where the second line's intensity was only 5% compared to the main line, for larger clusters the probability of second order effects is strongly enhanced. This is due to the fact that for larger clusters the probability for additional interactions of either the projectile or the ejected electron is enhanced due to the presence of a larger number of bound atoms and therefore a larger number of additional electrons. However, no calculations on such a reaction

[3]Similar with respect to the energy resolution.

channel could be found. Still, it can be argued that in particular the excitation of a $3p$ - electron in neutral Ar to a $2p_i$ - state[4] exhibits strong cross-sections. Futhermore, the fact that the neutral fragment is created by dissociation such a channel should be possible and in particular the absence of possible excitation in Ar_2 indicate that excited cluster states at those energies ($> 10\,\mathrm{eV}$) might not be stable at all.
Figure 4.14 shows the energy distribution of the ejected electron for an ejection angle of $\theta_{e2} = 90\,^\circ$ for Ar_n. As a comparison, the same distribution has been plotted for the ejected electron of Ar. The data is normalized to the respective integral value. It can be seen for energies below $E_{e2} = 3\,\mathrm{eV}$ the intensity for the electrons corresponding to the larger clusters increases compared to Ar. A similar behavior was observed in the single ionization of H_2 by 6 MeV proton impact [14]. In this experiment an increased intensity for the ejected electron distribution for energies below 1 eV was observed. The enhanced production of those sub-eV electrons was accounted to the existence of autoionization channels. This mechanism is explained by the excitation to a Rydberg state of one electron where the excited vibrational states are energetically above the ionization threshold. This process is therefore called *vibrational autoionization* and is referred to as an example where the Born-Oppenheimer approximation is no longer valid. In the case of larger argon clusters, however, it cannot finally be clarified whether this picture is appropriate or not. This is mainly due to the insufficient statistics and the limited acceptance of the spectrometer for electrons with energies below 1 eV.

For additional comparison the same distribution are plotted for argon dimers in figure 4.15. For energies above 10 eV dimers and larger clusters have the same characteristic and both are above the argon atom distribution. At $\sim 10\,\mathrm{eV}$ they part and the dimer distribution intersects with the atomic distribution and maintains a reduced intensity until an energy of 1 eV.

In figure 4.16 differential data can be seen, where the angle of the ejected electron θ_{e2} was plotted against the number of counts. The scattering angle of the projectile was integrated over $\theta_{e1} = 4 \ldots 25\,^\circ$ while the energy of the ejected electron was integrated over $E_{e2} = 1 \ldots 51\,\mathrm{eV}$. By comparing the intensity for the scattering plane and the perpendicular plane it is conspicuous that the number of counts exhibited in the perpendicular plane is much larger than in the case of Ar or Ar_2. This is a strong indication for higher order effects to occur in the ionization process. For instance – which was discussed for argon in section 2.1.1 and indicated in the context of inelastic scattering – due to the high core charge the probability for additional elastic scattering of either the projectile or the ejected electron increases. This leads to an overall increased cross-section in the perpendicular plane which was already observed for dimers. In a simple picture one can imagine that additional elastic scattering becomes more likely the more scattering centers are present.

[4] In Paschen notation.

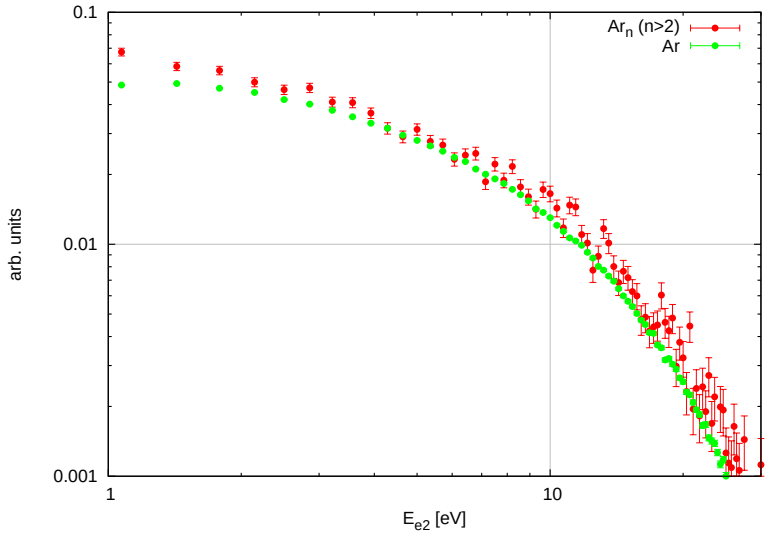

Figure 4.14.: Energy distribution of the ejected electron for an angle of $\theta_{e2} = 90\,°$. Plotted is Ar_n $(n > 2)$ (●) and Ar (●).

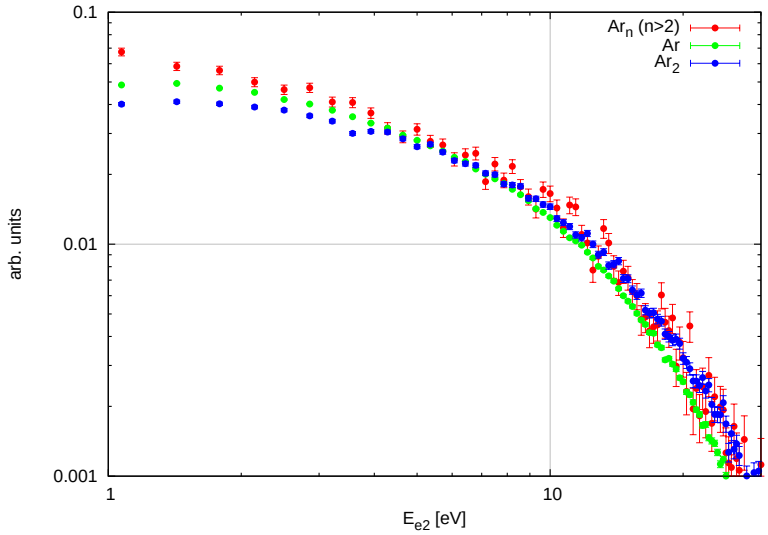

Figure 4.15.: Energy distributions of the ejected electron for an angle of $\theta_{e2} = 90\,°$. Plotted is Ar_n $(n > 2)$ (●) and Ar (●). For further comparison Ar_2 is plotted (●).

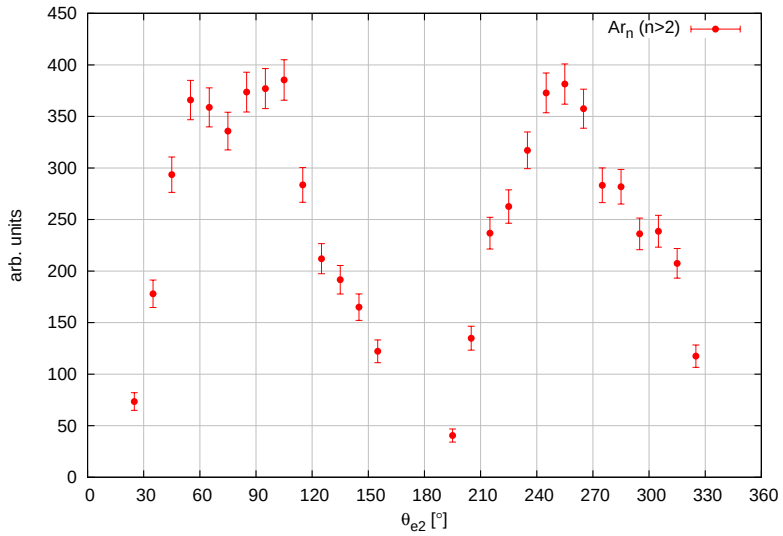

(a) Scattering plane.

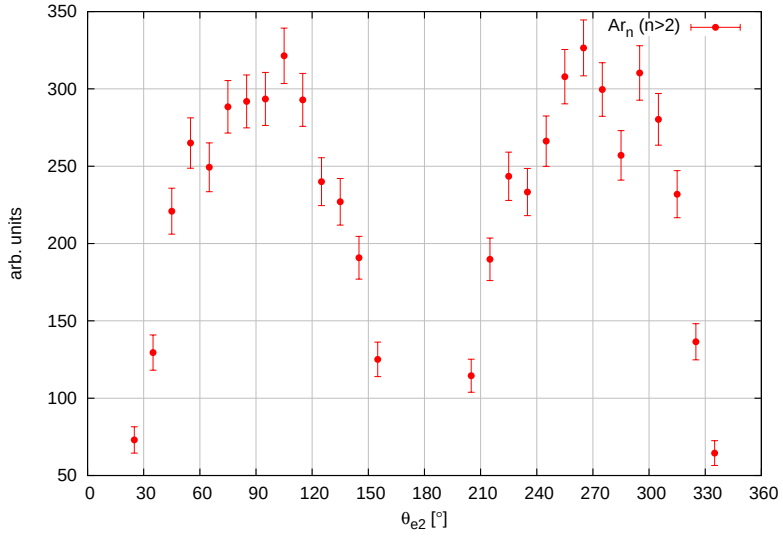

(b) Perpendicular plane.

Figure 4.16.: Differential cross-section for Ar_n ($n > 2$). The data have been integrated over a scattering angle of the projectile of $\theta_{e1} = 4 \ldots 25\,^\circ$ and an energy of the ejected electron of $E_{e2} = 1 \ldots 51\,\mathrm{eV}$.

5. Summary and Outlook

The main goal of the presented work is to present the first triply differential data for the single ionization of Ar_2 at a projectile energy of $E_0 = 100\,\mathrm{eV}$. The obtained cross-sections are compared to those for the single ionization of atomic argon at the same initial energy. Furthermore ionizing collisions on larger argon clusters are studied and differential data is obtained. The experimental setup used to acquire the data is described in detail in chapter 3. To ensure comparability all measurements were carried out under the same conditions with great effort to eliminate possible long term effects to be apparent for one target only. Amongst other things the different targets have been measured alternating before changing the experimental conditions. This method allows for the individual target to be close in time to the next whereas drifts that take place on a large time scale distribute equally over the targets targets and settings. A general overview of the underlying principles of $(e, 2e)$ experiments and a description of the considered targets as well as the expected characteristics within this measurement is given.

In a first step fully differential cross-sections of Ar are presented. It could be shown that the expected characteristic features for the ionization of argon are apparent. This includes the occurrence of higher order effects and the accordingly enhanced intensity in out-of-plane geometries such as the perpendicular plane. Furthermore, the suppression of ejected electrons with a momentum equal to the momentum transfer $\vec{q}$ is reproduced by the experiment. This feature is explained by the initial momentum of the $3p$ wave function. A comparison of the FDCS to contemporary DWB2-RM theory gives reasonable agreement with the measured data and can, in turn, reproduce the characteristics of the ionization process. Since the applied theory has well-known limitations – especially for low energetic collisions – such as an underestimation of the recoil peak it is shown that the more sophisticated 2nd Born approximation is a distinct improvement over the first order theory. Both models, however, show a large discrepancy with respect to the experimental data in the perpendicular plane. Since this deviation is not only in intensity but also of structural nature it must be considered that the described scattering process contains features which are – so far – not covered by the applied model.
Secondly, the TDCS for Ar_2 are shown and subsequently compared to those for Ar. The differences observable in the coplanar geometry are subtle and due to the obtained statistics for Ar_2 not finally presentable as significant. Since for a van-der-Waals molecule such as Ar_2 differences to atomic argon are expected to be

small – due to the weak intermolecular bond strength – is has been mentioned that non-coplanar geometries exhibit greater sensitivity for small deviations. In the perpendicular plane distinct differences in shape and intensity are visible. As assumed, the presence of a second bound atom leads to different emission patterns originating from an enhanced importance of higher order effects. The resulting difference leads to the conclusion that of the ejected electrons more are getting scattered out of the coplanar geometry due to additional elastic scattering processes. Furthermore, the distribution in the perpendicular plane is particularly enhanced in the backwards direction. Finally, the difference in the FDCS spectra indicate that argon dimers have to be looked at as real molecules and not as two independent atoms. This was even more apparent by looking at the energy distributions of the ejected electrons – or singly differential cross-sections – in Ar and Ar_2, respectively. It is shown that the two distributions intersect at $E_{e2} = 10\,\mathrm{eV}$, which corresponds to electrons with a de Broglie wavelength λ_B of the intermolecular equilibrium distance of the dimer nuclei. The corresponding theory is discussed in section 2.2.2 where it can be seen that the cross-sections are equal for a vanishing interference term. The same behavior is observed for Ar_2 being a strong indicator for interference. Since interference for inelastic scattering is only observable if the electrons are not localized, in this line of thought it must be clear that in the case of Ar_2 the electrons form real molecular orbitals.

For the ionization of larger clusters less differential data is shown. The cross-sections in the perpendicular plane show a large count rate, which exceeds the intensity for argon and argon dimers significantly. As for dimers it indicates the growing importance of higher order effects with increasing number of atoms participating in the formation of a cluster. The energy distribution of the ejected electron for a fixed ejection angle $\theta_{e2} = 90\,^\circ$ is first compared to the atomic argon case to provide a basis for further discussions. Overall the data corresponding to the ionization of larger clusters has a similar distribution compared to the atomic case. For low energetic electrons, however, the distribution for larger clusters exhibits a slightly increasing number of counts towards $E_{e2} = 1\,\mathrm{eV}$. A similar behavior has been observed for fast proton impact on H_2 and can be explained by the excitation to Ryberg states and followed by vibrational autoionization. Due to the restricted acceptance for slow electrons to energies of $E_{e2} > 1\,\mathrm{eV}$ and the limited statistics, this behavior cannot finally be clarified. Compared to the distribution for single ionization of Ar_2 both species show also a different characteristic towards small energies. While larger clusters show the just discussed enhancement dimers show a reduced count rate. Nevertheless, this is no prove that for dimers a similar increase for even smaller energies while the overall behavior for dimers – and therefore the difference to larger clusters – is explained by interference effects.

For all targets, additionally, energy loss spectra are plotted which show on one hand the ionization potential for direct ionization but on the other hand reveal higher order effects like simultaneous ionization/excitation. Such processes are visible for

argon where a simultaneous excitation to a $3d'$ or $4d$-state is observed which was also observed in an earlier experiment performed at an initial energy of $E_0 = 200\,\mathrm{eV}$. These states all have considerable cross-sections while, at the same time, the width of the measured line is larger than the main line. This is an indicator for excitation to multiple states because of the increasing resolution for lower energies. In neither of the two spectra an indicator is found for the ejection of a $3s$-electron. This is an interesting outcome since technically the latter would be a first order process. A second, but different, line is also apparent for the ionization of larger clusters which corresponds to a dissociative process where, for instance, Ar_3 gets ionized and dissociates into Ar_2^+ and an excited neutral argon. For the atom it corresponds to excitation to a $4p$-state which, again must be considered to be a multitude of different populated states due to the width of this line. However, the energy sum for argon dimers shows no indication of such a process. Since during the measurement of Ar_2 it wasn't possible to look for dissociation into Ar^+ and Ar a statement about a possible excitation of this neutral cannot be made. The width of all main lines are comparable so it is unlikely that the dimer was excited to states very close to its ground state and therefore it can be argued that states further away from the Ar_2^+ ground state dissociate.

The remaining open questions that could not be answered in the scope of this experiment turn out to be fruitful sources of ideas for further experiments. First and simplest the problem of the statistics for dimers and larger clusters could be addressed by a longer measurement time. Additionally, the creation of clusters could be enhanced by pre-cooling the target gas. This, of course, has to be done in a controlled manner to be able to specify the desired cluster size and not just produce larger and larger clusters. Since this method is rather incomplex in the sense of minor technical changes to the existing apparatus a more troubling issue concerning the ionization of larger clusters – being the actual size of which – can only be addressed by a real cluster source. Such a source would improve the experiment in many ways. Not only can one exclusively study a single desired cluster species, but also respective dissociation channels which cannot be assigned to a specific type with a mixed-sized target. A size-selective cluster source, however, has to ensure a reasonable target density otherwise the count rate will decrease rapidly.
In order to gain better resolution of the ion momenta, recently a larger ion detector was installed. It was positioned next to the spectrometer plates, thus reducing the distance to the reaction point of two-thirds. It is now possible to measure the ion TOF still with the TDC at high resolution, even for large clusters. This and the fact that due to the size of the detector dissociative processes several charged particles can be studied opens up possibilities for even more intersting experiments such as double ionization of argon dimers or larger clusters which is followed by coulomb explosion. Furthermore, as an improvement of the projectile beam a photoemission electron source is under construction and will enable projectile energies as low as a

few eV while maintaining a short pulse width and a narrow energy distribution. It will not only ensure an improved resolution but also create the possibility to perform measurements close to the ionization threshold which, in turn will be an interesting field of investigation for small noble gas clusters.
Lastly, since through the realization of this experiment a lot of knowledge has been gained about the topic it would be a logical step to study other noble gas clusters such as neon or xenon in the future.

A. Appendix

A.1. Time Focusing

The finite extension of the supersonic gas jet in the xz-plane makes it impossible to determine where within the extension the fragmentation took place. This leads to an uncertainty in the acceleration length and therefore to an uncertainty in the TOF of the particle which in turn projects to a momentum uncertainty. To overcome this problem a technique called *time focusing* is applied [40]. In the following it shall be discussed what time focusing is and in which way it can improve the resolution of the spectrometer.
Since the effect of variations in the drift length a is to be derived, it has to be pointed out that the extraction voltage is a function of the acceleration length, too. Therefore the following substitution $U = a \mid \vec{E} \mid$ is performed. In equation 3.6 the limit for small momenta (i.e. $\mid p_{\shortparallel} \mid \ll 1$ a.u.) is

$$t(p_{\shortparallel} = 0) = \sqrt{\frac{M}{2qa \mid \vec{E} \mid}} \cdot (2a + d) \; , \tag{A.1}$$

with q the charge, M the mass and $E = |\vec{E}|$ the electric field strength. The drift length is denoted by d.
This function has been plotted in figure A.1(a) for electrons and typical spectrometer values including $d = 0.22\,\mathrm{m}$.[1] The variation of the acceleration length $\Delta a = d/2 - a$ versus the relative TOF deviation is shown for zero momentum in figure A.1(a) while in figure A.1(b) the same function is plotted for the momenta $p_{\shortparallel} \in \{0, 0.5, 1\}$ a.u. (red, green, brown).
From figure A.1(a) it is obvious that equation A.1 has a minimum for

$$\frac{\mathrm{d}}{\mathrm{d}a} t \stackrel{!}{=} 0 \quad \Rightarrow \quad \boxed{a = \frac{d}{2}} \, . \tag{A.2}$$

Since the connection between drift length and acceleration length has been derived for zero longitudinal momentum, it is quite impressive the relative difference in the TOF is about two orders of magnitude and the behavior changes dramatically. With initial momentum the change in the TOF now changes the sign whether the reaction

[1] $E = 181.8\,\mathrm{V/m},\; m = 9.1 \cdot 10^{-31}\,\mathrm{kg}$

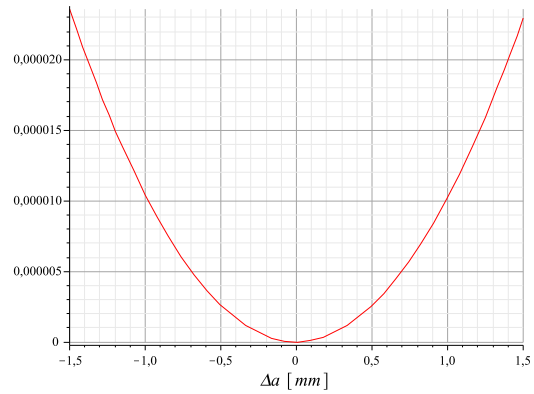

(a) Relative deviation of the electron TOF as a function of the acceleration length variation for $p_{\text{II}} = 0$ a.u. momentum.

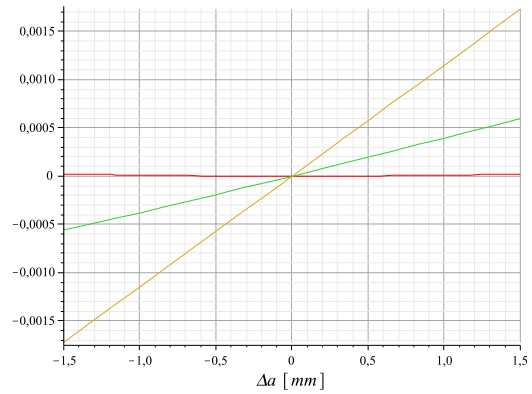

(b) Relative deviation of the electron TOF as a function of the acceleration length variation for $p_{\text{II}} \in \{0, 0.5, 1\}$ a.u. momentum (red, green, brown).

Figure A.1.: Acceleration length dependence of the TOF for electrons of various momenta.

took place before or after the center of the jet. Since the usual TOF for electrons in the ns regime the introduced uncertainty is still below the resolution of the TAC. Figure A.2 shows the relative acceleration length dependence for helium and several momenta. As one can see clearly is that because of the large mass (in respect to electrons), the deviation in the TOF is practically independent of the ion momentum. Secondly – in figure A.2(a) – on can see that for ions the time focusing gives reasonably good results. Compared to the electrons with initial momentum, the relative deviation of the ion TOF is two orders of magnitude smaller. Since the absolute ion TOF is in the μs regime the resulting uncertainty is reduced significantly and the behavior of the deviation doesn't change its sign like in the electron case. Therefore one can see that time focusing give good results for ions, even when initial momenta are introduced. The second plot – figure A.2(b) – shows helium for the same momenta but this time with drift length $d = 0$ mm. This can be of importance when studying molecular dissociation where the transversal momenta can become considerably large. Therefore it is of advantage to place the ion detector closer to the spectrometer plates without drift length to still be able to image the fragments. Furthermore, for heavy molecules the TOF can become quite large, thus exceeding the time range of the TAC. Shortening or excluding the drift length is therefore an advantage to reduce the TOF. The plot shows that deviation is now almost three orders of magnitude larger compared to the situation with drift length and – like for electrons – the TOF changes its sign with respect to the reaction point. Still – due to the mass – the deviation is independent of the relative change in time. The

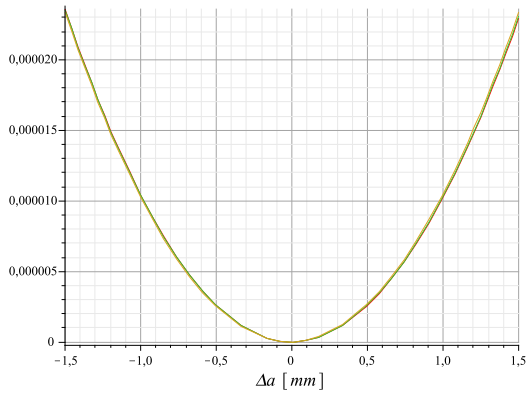

(a) relative deviation in acceleration length for helium with drift length

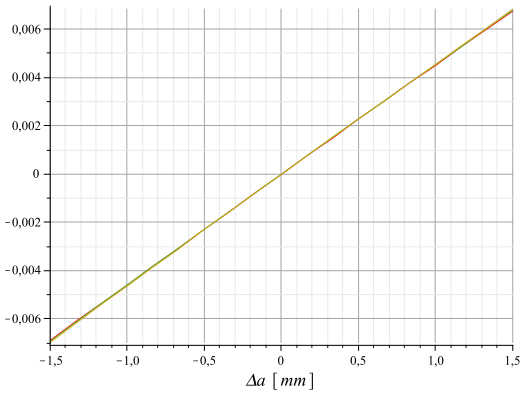

(b) relative deviation in accretion length for helium without drift length

Figure A.2.: Acceleration length dependence of the TOF for helium. The plot was done for momenta 0 a.u., 0.5 a.u. and 1 a.u.

introduced uncertainty, however, is measurable since it lies now in the ns regime. To still keep the time focusing condition while at the same time shortening the distance of the ion detector to the reaction point, a reduced acceleration length could be an appropriate solution. This would result in an asymmetric spectrometer for electrons and ions which, in turn, affects the applicable spectrometer voltage. There it is desired to have an overall low voltage for an increased resolution while the center of the spectrometer is usually on earth potential. To maintain this condition while reducing the acceleration length for the ions one has to make sure that the voltage on the ion side is still high enough to prevent electrons that hare scattered in the direction of the ion detector from entering the drift region of the ions.

A.2. Energy Levels of Ar I and Ar II

Ar I [33]

Configuration	Term	J	Level [cm^{-1}]	Level [eV]
$3p^6$	1S	0	0.0000	0.00
$3p^5(^2P_{3/2})\,4s$	2[3/2]	2	93143.7653	11.64
		1	93750.6031	11.72
$3p^5(^2P_{1/2})\,4s$	2[1/2]	0	94553.6705	11.82
		1	95399.8329	11.92
$3p^5(^2P_{3/2})\,4p$	2[1/2]	1	104102.1043	13.01
		0	107054.2773	13.38
$3p^5(^2P_{3/2})\,4p$	2[5/2]	3	105462.7649	13.18
		2	105617.2753	13.20
$3p^5(^2P_{3/2})\,4p$	2[3/2]	1	106087.2651	13.26
		2	106237.5571	13.28
$3p^5(^2P_{1/2})\,4p$	2[3/2]	1	107131.7139	13.39
		2	107289.7054	13.41
$3p^5(^2P_{1/2})\,4p$	2[1/2]	1	107496.4219	13.44
		0	108722.6247	13.59
$3p^5(^2P_{3/2})\,3d$	2[1/2]	0	111667.7710	13.96
		1	111818.0330	13.98
$3p^5(^2P_{3/2})\,3d$	2[3/2]	2	112138.9290	14.02
		1	114147.7370	14.27
$3p^5(^2P_{3/2})\,3d$	2[7/2]	4	112750.1580	14.09
		3	113020.3600	14.13
$3p^5(^2P_{3/2})\,3d$	2[5/2]	2	113425.9690	14.18
		3	113716.5600	14.21
$3p^5(^2P_{3/2})\,5s$	2[3/2]	2	113468.4780	14.18
		1	113643.2650	14.21
$3p^5(^2P_{1/2})\,3d$	2[5/2]	2	114640.9970	14.33
		3	114821.9440	14.35
$3p^5(^2P_{1/2})\,3d$	2[3/2]	2	114805.1400	14.35
		1	115366.8710	14.42
$3p^5(^2P_{1/2})\,5s$	2[1/2]	0	114861.6400	14.36
		1	114975.0240	14.37

Ar II [33]

Configuration	Term	J	Level [cm^{-1}]	Level [eV]
$3s^2 3p^5$	^2P	3/2	0.0000	0.00
		1/2	1431.58	0.18
$3s 3p^6$	^2S	1/2	108721.53	13.59
$3s^2 3p^4(^3P)\,3d$	^4D	7/2	132327.36	16.54
		5/2	132481.21	16.56
		3/2	132630.73	16.58
		1/2	132737.70	16.59
$3s^2 3p^4(^3P)\,4s$	^4P	5/2	134241.74	16.78
		3/2	135086.00	16.89
		1/2	135601.73	16.95
$3s^2 3p^4(^3P)\,4s$	^2P	3/2	138243.64	17.28
		1/2	139258.34	17.41
$3s^2 3p^4(^3P)\,3d$	^4F	9/2	142186.32	17.77
		7/2	142717.10	17.84
		5/2	143107.68	17.89
		3/2	143371.44	17.92
$3s^2 3p^4(^1D)\,4s$	^2D	3/2	148620.14	18.58
		5/2	148842.47	18.61
$3s^2 3p^4(^3P)\,3d$	^2D	3/2	150474.99	18.81
		5/2	151087.31	18.89
$3s^2 3p^4(^3P)\,4p$	^4P	5/2	155043.16	19.38
		3/2	155351.12	19.42
		1/2	155708.11	19.46
$3s^2 3p^4(^3P)\,4p$	^4D	7/2	157234.02	19.65
		5/2	157673.41	19.71
		3/2	158167.80	19.77
		1/2	158428.11	19.80
$3s^2 3p^4(^3P)\,4p$	^2D	5/2	158730.30	19.84
		3/2	159393.39	19.92
$3s^2 3p^4(^3P)\,4p$	^2P	1/2	159706.53	19.96
		3/2	160239.43	20.03
$3s^2 3p^4(^1D)\,4p$	^2F	5/2	170401.02	21.30
		7/2	170530.40	21.32
$3s^2 3p^4(^1D)\,4p$	^2P	3/2	172213.88	21.53
		1/2	172816.29	21.60

A.3. Atomic Units

Physical Quantity	a.u.	SI-units		special
mass	m_e	$9.1094 \cdot 10^{-31}$	kg	
angular momentum	$\hbar$	$1.0546 \cdot 10^{-34}$	Js	
charge	e	$1.6022 \cdot 10^{-19}$	C	
length	$a_0 := \frac{4\pi\epsilon_0\hbar}{m_e e^2}$	$5.2918 \cdot 10^{-11}$	m	
energy	$E_h := \frac{\hbar^2}{a_0^2 m_e}$	$4.3597 \cdot 10^{-18}$	J	27.2141 eV
time	$\frac{\hbar}{E_h}$	$2.4189 \cdot 10^{-17}$	s	
velocity	$v_0 := \frac{a_0 E_h}{\hbar}$	$2.1877 \cdot 10^{6}$	ms^{-1}	
momentum	$m_e v_0$	$1.9929 \cdot 10^{-24}$	kgms^{-1}	
el. potential	$\frac{E_h}{e}$	27.211	V	

Usefull Conversions

$$p[\text{a.u.}] = 0.27 \cdot \sqrt{E[\text{eV}]} \qquad \text{(electron momentum)}$$

$$E[\text{eV}] = 125 \cdot 10^{-6}\ \bar{\nu}\,[\text{cm}^{-1}] \qquad \text{(wavenumber conversion)}$$

$$r_e[\text{mm}] = 33.7 \cdot \frac{\sqrt{E[\text{eV}]}}{B[\text{Gs}]} \qquad \text{(cyclotron diameter for electrons)}$$

Bibliography

[1] Achtelik, A. *Aufbau eines gepulsten Überschall-Gasjet-Targets für hochauflösende Rückstoßionen-Impulsspektroskopie.* Diplomarbeit, Rupprecht-Karls-University of Heidelberg, 2008.

[2] Ballentine, L. *Quantum Mechanics: A modern development.* World Scientific Publishing Company, 1998.

[3] Bartschart, K., Bray, I., Fursa, D., and Stelbovics, A. Absolute triple-differential cross sections for ionization-excitation of helium. *Phys. Rev. A 76* (2007), 024703.

[4] Bastida, A., Halberstadt, N., Beswick, J., Gadea, F., Buck, U., Galonska, R., and Lauenstein, C. Electron impact ionization of small argon clusters. *Chem. Phys. Lett. 249* (1996), 1–6.

[5] Bencze, G. Impossibility of distinguishing between identical particles in quantum collision processes. *Phys. Rev. A 59* (1998), 3129.

[6] Bonhommeau, D., Halberstadt, N., and Viel, A. Fragmentation dynamics of argon clusters (Ar_n, n=2 to 11) following electron impact ionization: Modeling and comparison with experiment. *J. Chem. Phys 128* (2006), 184314.

[7] Bray, I., and Fursa, D. Calculation of ionization within the close-coupling formalism. *Phys. Rev. A 54* (1996), 2991.

[8] Buck, U., Meyer, H., and Pauly, H. Clusterformation in supersonic nozzle beams. In *Flow of Real Fluids*, vol. 235 of *Lecture Notes in Physics*. Springer, 1985, pp. 170–178.

[9] Chilton, J., Boffard, J., Schappe, R., and Lin, C. Mesurement of the electron-impact excitation into $3p^5 4p$ levels of argon using Fourier-transform spectroscopy. *Phys. Rev. A 57* (1998), 267.

[10] Chilton, J., Boffard, J., Schappe, R., and Lin, C. Measurement of electron-impact excitation into the $3p^5 3d$ and $3p^5 5s$ levels of argon using Fourier-transform spectroscopy. *Phys. Rev. A 60* (1999), 3712.

[11] Cohen, H., and Fano, U. Interference in the photo-ionization of molecules. *Phys. Rev. 150* (1966), 30.

[12] Danica, C., and Crowe, A. Differential cross sections for elastic scattering of electrons from argon and krypton as a continuous fuction of energy. *J. Phys. B 30* (1997), 2873.

[13] Demtröder, W. *Molekülphysik.* Oldenburg, 2003.

[14] Dimopoulou, C., Moshammer, R., Fischer, D., Höhr, C., Dorn, A., Fainstein, P., Crespo Lopéz Urrutia, J., Schröter, C., Kollmus, H., Mann, R., Hagmann, S., and Ullrich, J. Breakup of H_2 in singly ionizing collisions with fast protons: Channel-selective low-energy electron spectra. *Phys. Rev. Lett. 93* (2004), 123203.

[15] Duerr, M. *Electron Induced Break-up of Helium: Benchmark Experiments on a Dynamical Four-Body Coulomb System.* PhD thesis, Rupprecht-Karls-University of Heidelberg, 2006.

[16] Dürr, M., Dimopoulou, C., Najjari, B., Dorn, A., and Ullrich, J. Three-dimensional images for electron-impact single ionization of He: Complete and comprehensive (e, 2e) benchmark data. *Phys. Rev. Lett. 96* (2006), 243202.

[17] Ehrhardt, H., Schulz, M., Tekaat, T., and Willmann, K. Ionization of helium: Angular correlation of the scattered and the ejected electrons. *Phys. Rev. Lett. 22* (1969), 89.

[18] Gonzales-Lezana, T., Rubayo-Soneira, J., Miret-Atres, S., Gianturco, F., Delgado, G., and Villarreal, P. Comparative configurational study for He, Ne, and Ar trimers. *J. Chem. Phys. 110* (1993), 9000.

[19] Gorfinkiel, J., and Tennyson, J. Electron impact ionisation of small molecules at intermediate energies: the molecular R-matrix with pseudostates method. *J. Phys. B 38* (2005), 1607.

[20] Haag, N. *Kinematisch vollständige Experimente zur elektronenstoßinduzierten Ionisation und Dissoziation von H_2-Molekülen.* Diplomarbeit, Rupprecht-Karls-University of Heidelberg, 2006.

[21] Ikegami, T., and Kondow, T. The geometric and electronic structures of Ar_n^+ (n=3-27). *J. Chem. Phys. 98* (1993), 3038.

[22] Jha, L., Kumar, S., and Roy, B. Electron impact single and double ionization of argon. *Eur. Phys. J. D 40* (2006), 101.

[23] Jönsson, C. Elektroneninterferenz an mehreren künstlich hergestellten Feinspalten. *Zeitschrift für Physik A 161* (1961), 454.

[24] Kahkoo, M., Vandeveter, P., Childer, J., Kanik, I., Fontes, C., Bartschat, K., Zeman, V., Madison, D., Saxena, S., Srivastara, S., and Stauffer, A. Electron impact excitation of the argon $3p^5 4s$ configuration: differential cross-sections and cross-section ratios. *J. Phys. B 37* (2004), 247.

[25] Kheifets, A., Naja, A., Staicu-Cassagrande, E., and Lahmam-Bennani, A. DWBA-G calculations of electron impact ionization of noble gas atoms. *J. Phys. B 41* (2008), 145201.

[26] Kraft, T., Bregel, T., Ganz, J., Harth, K., Ruf, M., and Hotop, H. Accurate comparison of HeI, NeI photoionization and He($2^{3,1}S$), Ne($3s^3P_2$, $^3P_0$) penning ionization of argon atoms and dimers. *Z. Phys. D 10* (1988), 473.

[27] Kuntz, P., and Valldorf, J. A DIM model for homogeneous noble gas ionic clusters. *Z. Phys. D 8* (1988), 195.

[28] McCallion, P., Shah, M., and Gilbody, H. A crossed beam study of the multiple ionization of argon by electron impact. *J. Phys. B 25* (1991), 1061.

[29] Miller, D. Free jet sources. In *Atomic and Molecular Beam Methods*. Oxford University Press, 1988, pp. 14–53.

[30] Moshammer, R., Fischer, D., and Kollmus, H. Recoil-ion momentum spectroscopy and "reaction microscopes". In *Many-Particle Quantum Dynamics in Atomic and Molecular Fragmentation*, J. Ullrich and V. Shevelko, Eds. Springer, 2003.

[31] Moshammer, R., Unverzagt, M., Schmitt, W., Ullrich, J., and Schmidt-Böcking, H. A 4π recoil-ion electron momentum analyzer: A high-resolution 'microscope' for the investigation of the dynamics of atomic, molecular and nuclear reactions. *Nucl. Instrum. Methods B 108* (1996), 425–445.

[32] Sakurai, J. *Modern Quantum Mechanics*. Addison-Wesley, 1994.

[33] Sansonetti, J., and Martin, W. NIST - National Institute of Standards and Technology. website, 2005. Available online at `http://physics.nist.gov/PhysRefData/Handbook/index.html`.

[34] Schulz, M., Moshammer, R., Fischer, D., Kollmus, H., Madison, D., Jones, S., and Ullrich, J. Three-dimensional imaging of atomic four-body processes. *Nature 422* (2003), 48.

[35] Stelbovics, A., Bray, I., Fursa, D., and Bartschat, K. Electron-impact ionization of helium for equal-energy-sharing kinematics. *Phys. Rev. A 71* (2005), 052716.

[36] Stia, C., Fojón, O., Weck, P., Hanssen, J., and Rivarola, R. Interference effects in single ionization of molecular hydrogen by electron impact. *J. Phys. B 36* (2003), L257.

[37] Stolterfoth, N., Sulik, B., Hoffmann, V., Skogvall, B., Chesnel, J., Rangama, J., Frémont, F., Hennecart, D., Cassimi, A., Husson, X., Landers, L., Tanis, J., Galassi, M., and Rivarola, R. Evidence for interference effects in electron emission from H_2 colliding with 60 MeV/u Kr^{34+} ions. *Phys. Rev. Lett. 87* (2001), 023201.

[38] Tan, K.-H., and McConkey, J. Simultaneous ionization and excitation of Ar by electrons with particular attention to configuration-interaction effects. *Phys. Rev. A 10* (1074), 1212.

[39] Wadt, W. The electronic states of Ar_2^+, Kr_2^+, Xe_2^+. I. Potential curves with and without spin-orbit coupling. *J. Chem. Phys 68* (1978), 402.

[40] Wiley, W., and McLaren, I. Time-of-flight mass spectrometer with improved resolution. *Rev. Scient. Instrum. 26* (1955), 1055.

Erklärung:

Hiermit versichere ich, dass ich die vorliegende Arbeit selbstständing verfasst und keine anderen als die angegebenen Quellen als Hilfsmittel verwendet habe.

Heidelberg, _____ _____

Unterschrift